IMAGE: A MAP OF THE STARS OF THE ORION CONSTELLATION

Print ISSN: 2631-8474 Online ISSN: 2631-8482

JournalPreview

London Journal of Engineering Research

Volume 23 | Issue 5 | Compilation 1.0

Great Britain
Journals Press

WWW.JOURNALSPRESS.COM

JournalPreview

LONDON JOURNAL ENGINEERING RESEARCH

Journal Content

In this Issue

Great Britain
Journals Press

Behavior of Laterally Top-Loaded Drilled Piles in Collapsible Tropical Soil

Albuquerque, Paulo José Rocha & Carvalho, David

Universidade Estadual

ABSTRACT

Among the various types of loading to which foundations are subject, one can single out transversal (horizontal) forces. In general terms, we notice a lack of knowledge on the parameters used to design pile foundations with this type of load which will stress surface soil, considering that tropical soils are very often collapsible.

Aiming to furnish input for future geotechnical projects, transversal loading tests were performed on a bored pile and a continuous flight auger (CFA) pile, both 12.0 m in length, and 0.40 m in diameter. The loading tests were performed with the soil in its natural condition and by pre-flooding the area, at the UNICAMP (Universidade Estadual de Campinas) Experimental Soil Mechanics and Foundations Field I in Campinas/SP, Brazil, where the unsaturated soil is porous and classified as silty-sandy clay. The edometric tests indicated that is a collapsible soil in the surface bed up to 6.5m, and that the reduction in pre-collapse stress in the flooded condition is of the order of three times that of the natural condition. The load tests indicated that the maximum load in the natural condition is five times higher than in the flooded condition and that the value of nh (horizontal reaction coefficient) reduces substantially with the effect of increasing soil moisture content.

Classification: LCC Code: TA775

Language: English

Great Britain
Journals Press

LJP Copyright ID: 392921
Print ISSN: 2631-8474
Online ISSN: 2631-8482

London Journal of Engineering Research

Volume 23 | Issue 5 | Compilation 1.0

Behavior of Laterally Top-Loaded Drilled Piles in Collapsible Tropical Soil

Albuquerque, Paulo José Rocha[α] & Carvalho, David[σ]

ABSTRACT

Among the various types of loading to which foundations are subject, one can single out transversal (horizontal) forces. In general terms, we notice a lack of knowledge on the parameters used to design pile foundations with this type of load which will stress surface soil, considering that tropical soils are very often collapsible.

Aiming to furnish input for future geotechnical projects, transversal loading tests were performed on a bored pile and a continuous flight auger (CFA) pile, both 12.0 m in length, and 0.40 m in diameter. The loading tests were performed with the soil in its natural condition and by pre-flooding the area, at the UNICAMP (Universidade Estadual de Campinas) Experimental Soil Mechanics and Foundations Field I in Campinas/SP, Brazil, where the unsaturated soil is porous and classified as silty-sandy clay. The edometric tests indicated that is a collapsible soil in the surface bed up to 6.5m, and that the reduction in pre-collapse stress in the flooded condition is of the order of three times that of the natural condition. The load tests indicated that the maximum load in the natural condition is five times higher than in the flooded condition and that the value of n_h *(horizontal reaction coefficient) reduces substantially with the effect of increasing soil moisture content.*

Author α: PhD, Full Professor, Universidade Estadual de Campinas - UNICAMP, FECFAU, Campinas/SP.
σ: PhD, Associate Professor, Universidade Estadual de Campinas - UNICAMP, Feagri, Campinas/ SP.

I. INTRODUCTION

Horizontal load situations are frequent in foundations, but the technical community is largely unaware of the properties of collapsible tropical soils when it comes to designing piles subjected to this effort (Albuquerque et al., 2019). This paper aims to fill part of the existing gap on this subject by obtaining valid parameters for the tropical collapsible soil common to the city of Campinas and other regions of Brazil, by carrying out horizontal load tests on drilled piles in the soil in the natural and flooded condition. This type of loading, in which the loading are often variable and cyclical, is also combined in some situations with tensile and compressive stresses.

Simplified mathematical models (Miche, 1930; Matlock and Reese, 1961; Broms, 1964; Poulos, 1971; Poulos and Davis 1980;) were created for analysis of transversal loads, since the modeling problems is three-dimensional and conventional solutions for project developers are extremely complex. The best-known and most widely used theory for evaluating these effects is the "horizontal reaction theory of soil", where the n_h factor represents the ratio between the reaction and displacement acting on the soil mass (Terzaghi, 1955; Palmer and Thompson, 1948; Davidson and Gill, 1963; Matlock and Reese, 1960, 1961; Davidson, 1970, Rosendo and Albuquerque, 2021; García et al, 2023). However, it is theoretically difficult to estimate this factor. However, it can be determined by load testing to obtain a reliable value for the transversal resistance of the construction soil.

The presence of collapsible soils is common in many regions of Brazil. Considering that these layers of collapsible soils can reach a depth of several meters and that the topsoil performs an important role in the behavior of transversely loaded piles, it is important to analyze the effect of this characteristic on the behavior of deep foundations. Analysis of the collapse potential is a very important factor to verify, as it most often dictates the behavior of unsaturated soils.

Collapsible soils are characterized by their high porosity and low degree of saturation and, through a process of increasing moisture content, suffer sudden and large additional deformations under constant total stresses.

Jennings and Knight (1957) provide a hypothesis for the phenomenon of collapse: the structure of a collapsible soil, when loaded at its natural moisture content, compresses smoothly, with no appreciable change in volume, resisting the compressive stresses between the grains, with no large relative movements between them. However, when this loaded soil gains moisture and reaches a critical moisture content, the bonds of resistance weaken and the structure collapses.

The grains or micro-aggregations are kept stable by the presence of suction (capillary and adsorption forces) and/or cementing agents (oxides, iron and/or aluminum hydroxides and carbonates). When these soils are moistened, these structure-stabilizing forces lose their intensity, allowing relative displacement between the particles, so that they begin to occupy the empty spaces in the soil structure (Dudley, 1970).

Thus, in order to provide parameters for the geotechnical environment, horizontal load tests were carried out at UNICAMP's Experimental Field of Soil Mechanics and Foundations I with natural and pre-flooded soil, with the aim of verifying the effect of collapsibility on the behavior of drilled piles (bored and CFA).

II. GEOTECHICAL AND GEOLOGICAL CHARACTERISTICS

This research was carried out at the Experimental Field for Soil Mechanics and Foundations I, located on the UNICAMP Campus (coordinates: -22.81937, -47.06047). Various in-situ and laboratory tests were carried out on disturbed and undisturbed samples. According to Carvalho et. al. (2000), the region's subsoil is formed by basic magmatites, with basic intrusive rocks from the Serra Geral Formation (diabase). They make up 98 km^2 of the Campinas region, occupying 14% of the total area. The profile of the Experimental Field is made up of diabase soil, with a surface layer 6.5 m thick made up of high-porosity sandy-silty clay followed by a layer of sandy-clay silt up to 17 m. The water table level is found between 13 m and 16 m, depending on the time of year. It can be said that the first layer is made up of mature soil which has undergone an intense weathering process. The phenomenon of leaching may explain the porosity, due to the transport of fines to the deeper horizon. The second layer is formed by a young residual soil, which retains characteristics inherited from the original rock. Figure 1 shows the geotechnical profile obtained from the SPT and CPT tests and Table 2 shows the average parameters obtained from the laboratory tests.

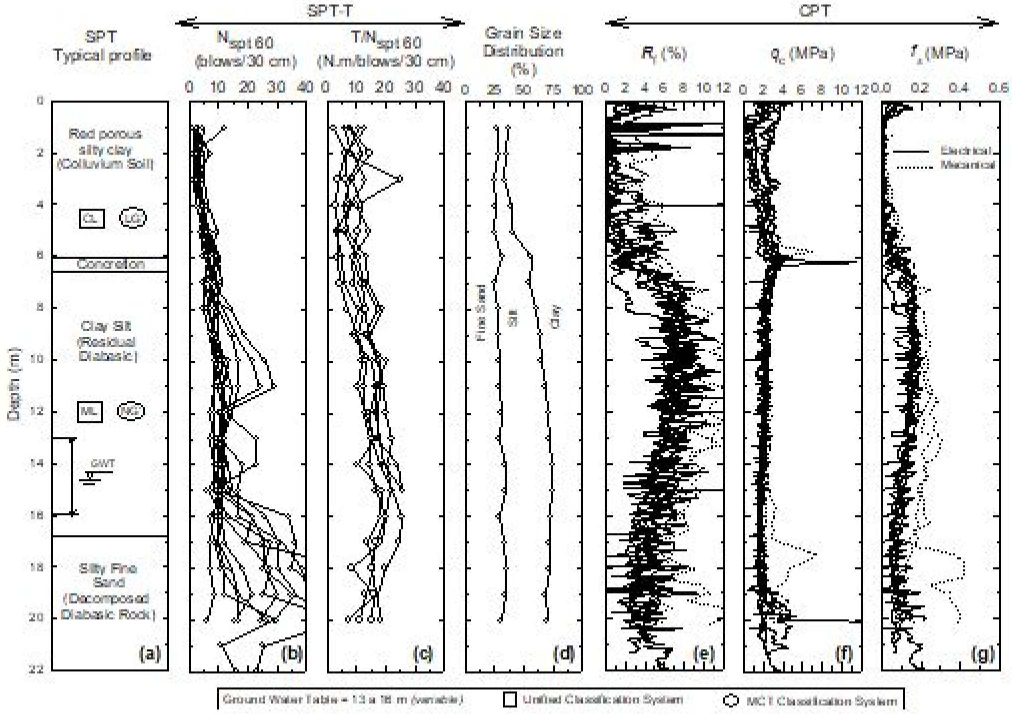

Figure 1: SPT-T and CPT (Electrical) Tests Results (Albuquerque et al, 2011)

Table 1: Average Physical Index Values

Layer	w (%)	e	n (%)	S_r (%)
0 → 6.5m	23.8	1.72	63.1	41.4
6.5 → 14m	30.3	1.52	54.6	59.6

w: natural soil moisture, e: initial void index, n: porosity, Sr: saturation degree,

In order to identify the potential for collapse, conventional and simple edometric tests were carried out, without suction control, in accordance with the procedures adopted from ASTM D 2435-04. In order to define the collapsibility of the surface layer, samples were taken at depths between 1.5 m and 6.5 m to be subjected to oedometer tests with and without pre-flooding. The loading stress values adopted were 13 kPa, 25 kPa, 50 kPa, 100 kPa, 200 kPa, 400 kPa, 800 kPa and 1600 kPa. Test specimens were molded from samples collected at depths of 1.5 m, 2.5 m, 4.5 m and 5.5 m.

The criterion adopted to quantify the collapse index (R_w) was that of Vargas (1978), according to expression (1). Thee and the soil is considered collapsible when its value is greater than 2%.

$$R_w = \left(\frac{e_p - e_w}{1 + e_p} \right) \times 100 \tag{1}$$

where:

R_w : subsidence index;
e_w : void ratio after flooding the test specimen;
e_p : void ratio before flooding the test specimen.

Due to the heterogeneity of the samples, represented by the different initial void ratio values (Table 2).

Table 2: Values of the Void Index

	Sample Depth			
	1.5 m	2.5 m	4.5 m	5.5 m
e_o	2.14	1.74	1.72	1.66

The results of the tests in saturated and unsaturated conditions are shown in Table 3.

Table 3: Pre-Consolidation Stress Values (Natural and Flooded)

Depth (m)	Pre-Consolidation Stress $\sigma_{av'}$(kPa) Flooded	Pre-Consolidation Stress $\sigma_{av'}$(kPa) Natural	$\sigma_{av'flooded}$ / $\sigma_{av'natural}$
1.5	18	63	0.29
2.5	30	110	0.27
4.5	110	230	0.48
5.5	105	300	0.35

Table 3 shows a reduction in the pre-consolidation stress in the flooded condition, with the reduction varying from 1/3 to 1/2 of the value of the stress in the natural condition. This behavior is related to the influence of the soil's initial moisture conditions, which in turn are closely linked to the suction values. When moistened, these soils lose the resistance between grains or micro-aggregates given by matric suction, as well as having their bonds due to cementation weakened by the increase in moisture and, jointly, with the application and magnitude of the load.

Figure 2 shows that the samples presented collapsible behavior, with collapse index values greater than 2% at all flood loads (except for sample 4.5 m flooded at load 50 kPa). The R_w values practically increase with the increase in loading, but tend to stabilize as the depth increases.

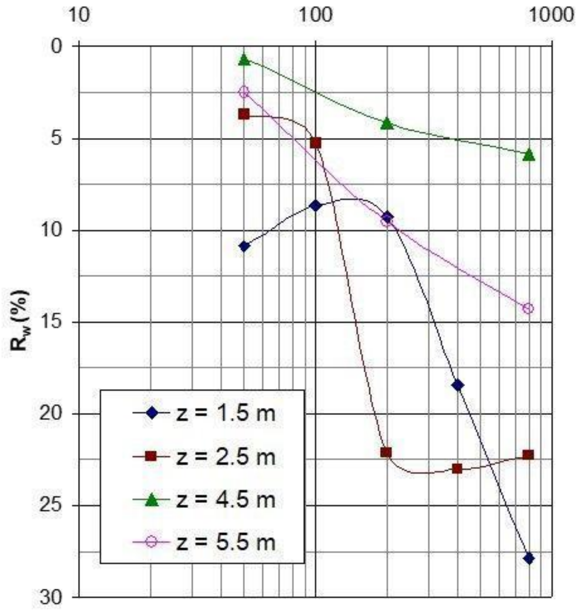

Figure 2: Collapse Index *vs* Logσ

The values in Tables 2 and 3 and the collapse index (R_w), as a function of flood stress, shown in Figure 2, the relationship between the values of pre-consolidation stress (virtual or yield) and R_w is striking. In other words, as the values of this stress increase, the collapse index values decrease and tend to stabilize.

Overall, the information obtained from CPTu and SPT-T tests, regarding soil type and resistance parameters in unsaturated conditions, allows to state that the soil in the experimental field is of low resistance and high collapsibility.

III. PILE CONSTRUCTION AND LOAD TESTS

The study used a bored pile with a diameter of 0.40 m and a depth of 12 m, and a continuous flight auger (CFA) pile with the same dimensions.

The longitudinal reinforcement of the piles consisted of $4\varphi_b$ 16.0mm ($\cong 8\ cm^2$), 6 m long and stirrups of $\varphi_b = 6.4$mm, every 20 cm (CA-50 steel).

For the bored piles, the concrete fck (slump ± 70mm) was around 15 MPa, using gravel and sand. The concrete used in the continuous auger pile (pumpable, slump ± 240mm) consumed cement at a rate of 400 kg/m³ and aggregates (sand and gravel). The CFA pile was drilled using the MAIT HR-200 drill rig, which can drill diameters of up to 1200 mm and depths of up to 32m. The piles followed a predefined alignment and the spacing between them was 2.4m (6φ).

The following elements were used to carry out the load tests: a 100 kN hydraulic jack, a 100 kN load cell, two deflectometers with a precision of 0.01 mm and a kneecap. All these elements were hollow and to prevent the system from becoming unstable during the tests, a steel bar was passed between them and fitted into two recesses made in the piles (Figures 3 and 4).

Figure 3: View of the Load Test Assembly

Figure 4: Assembly Detail

The load tests were of the quick maintained load (QML), following the requirements of NBR 12.131/1991. The load increments were 3 kN for the load test with natural soil and 2 kN for the pre-flooded situation. Unloading was carried out at predetermined intervals. Two loading and unloading cycles were carried out.

VI. RESULTS AND ANALYZES

The results obtained from the load tests are presented below, two (first and second) with the soil in its natural condition and the third after pre-flooding the ground for a period of 72 hours. Table 4 shows a summary of the results of the load tests carried out.

Table 4: Load and Displacement Maximum Values

Pile	Condition	Load (kN)	Displacement (mm)
Bored	Natural – 1st	54.0	7.82
	Natural – 2nd	67.5	21.20
	Flooded	13.0	13.66
CFA	Natural – 1st	54.5	11.02
	Natural – 2nd	67.5	33.76
	Flooded	13.0	30,26

The figures 5a and 5b show the load *vs.* displacement curves, with the first and second cycles and with pre-flooding of the ground. Using the methodology proposed by Matlock and Reese (1961), figures 6a and 6b show the horizontal reaction curves of the soil (n_h) *vs.* displacement of the pile on the ground surface (y_o), obtained from the results of the tests carried out with the soil in its natural and flooded condition, assuming that the horizontal reaction modulus of the soil varies linearly with depth. For the case of the piles under analysis, n_h was defined. for the 6.0 to 12.0mm range (Table 4).

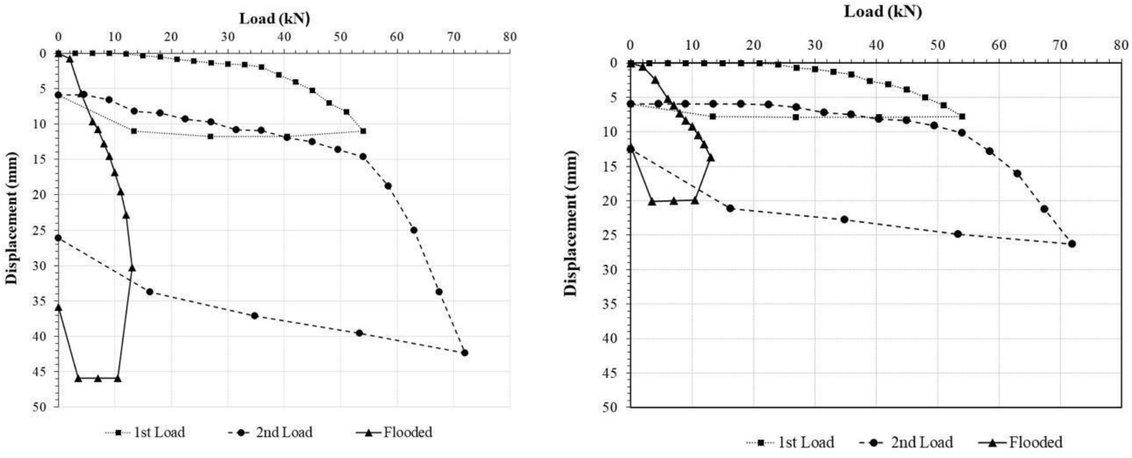

a) CFA Pile

b) Bored Pile

Figure 5: Load *vs.* Displacement Curve

The Figures 5a and 5b show that the pre-flooding of the soil caused a pronounced increase in the displacements for the same load applied in the tests with natural soil. The results proved that the pre-flooding caused a reduction of the applied load by 2.5 to 3.0 times when compared to the natural ultimate load. These results demonstrate the intensity of the effect of the variation of the soil moisture on the horizontal displacement characteristics of the pile.

In the third loading, with the soil already flooded, there is a large loss of bearing capacity of the pile, showing the effect of the collapsible characteristic of the soil in this type of loading. For the same value of maximum displacement as the second loading, there is a reduction in the bearing capacity of the soil of 85% in the third loading, with the soil pre-flooded.

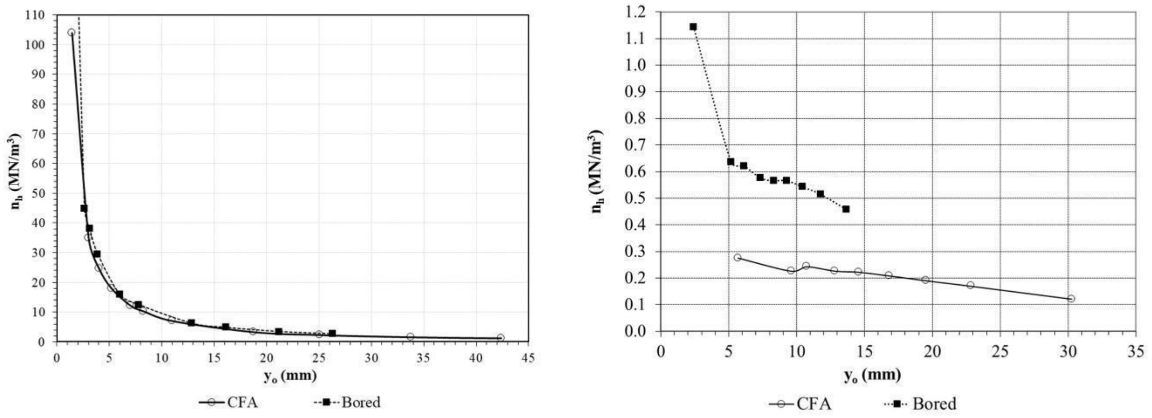

a) Natural

b) Flooded

Figure 6: n_h *vs* y_o Curves– Natural and Flooded

It can be seen in Figure 6a that the behavior of the n_h *vs* y_o curves were very similar for the two types of pile, showing that the soil reaction did not vary, even though they were two different types of pile construction processes. The horizontal reaction coefficient (natural moisture) for the bored pile was 11.8 MN/m³ and for the CFA pile 10.3MN/m³. Note that the n_h values in the pre-flooded situation practically do not vary, which demonstrates a resistance loss of the soil from the beginning of loading (Figure 6b).

The values of the horizontal soil reaction coefficient n_h, obtained for displacements of 6 to 12mm, are shown in Table 5.

Table 5: n_h values

Pile	Condition	n_h (MN/m³)	Condition	n_h (MN/m³)
Bored	Natural	11.8	Flooded	0.58
CFA	Natural	10.3	Flooded	0.24

The values for the horizontal reaction coefficients obtained in the literature for different types of deep foundations built on soil with similar behavior to the one from the present study (under natural and pre-flooded conditions) (Kassouf, Carvalho and Albuquerque, 2016; Barbosa et al., 2023)

IIV. CONCLUSIONS

- The oedometer tests showed that the deformations in the samples after being subjected to the tests were characterized, firstly, by the closure of the pores, and then by the sliding of the microaggregates (lumps), in this case, under the tension of 800kPa.
- Since the first meter of soil has a strong influence on horizontal loading, proper geotechnical characterization in terms of porosity, resistance and collapsibility is important. Laboratory and field tests indicate that soils are highly porous, low resistance collapsible soils, making it possible to predict the large effects of low n_h values and changes in soil moisture content.
- It has been observed that loads on pre-flooded soils are on average three times lower than soils with natural moisture content until a certain level of displacement is reached. For the soil horizontal reaction coefficient, the pre-flooded values are about 50% lower than those for the natural moisture content of the soil.
- The average horizontal reaction coefficient obtained for soils at natural moisture content is 11 MN/m³, which is higher compared to the literature for high porosity soils, where the recommended value is 2 MN/m³, emphasizing the importance of its determination for each soil type, to avoid generalizations. In the

flooded condition, the soil horizontal reaction coefficient showed an average reduction of approximately 96 % when compared to the natural condition.

- The results indicate that, after loading, there is little recovery of the displacement occurred by the pile during unloading. In a second loading, until the maximum load of the first loading is reached, the pile suffers little displacement. From this maximum load onwards, in the second loading, the curve takes on the continuity of the curve from the first loading, as can be seen in figure 5.

ACKNOWLEDGMENTS

The authors gratefully acknowledge to the support of the Universidade Estadual de Campinas (UNICAMP).

REFERENCES

1. ABNT NBR 12.131 (1991) Static load test (*in portuguese*).
2. Albuquerque, P.J.R.; Carvalho, D.; Kassouf, R., Fonte Jr., N.L. (2019) Behavior of Laterally Top-Loaded Deep Foundations in Highly Porous and Collapsible Soil. Journal of Materials in Civil Engineering. V.31 -2. https://doi.org/10.1061/(ASCE)MT.1943-5533.00025.
3. Albuquerque, P.J.R.; Massad, F., Viana da Fonseca, A.; Carvalho, D.; Santos, J.; Esteves, E.C. (2011) Effects of the construction method on pile performance: evaluation by instrumentation. part 1: experimental site at the State University of Campinas. V.34(1): 35-50, January-April. https://doi.org/10.28927/SR.341035.
4. ASTM D 2435 (2004) Standard test methods for one-dimensional consolidation properties of soils using incremental loading.
5. Barbosa, Y., Tarozzo, M.H.P.; Albuquerque, P.J.R. and Carvalho, D., (2023) Behavior of a new laterally top-loaded post-grouted micropile in highly porous lateritic soil. DYNA, 90 (225), pp. 123-131, January – March. https://doi.org/10.15446/dyna.v90n225.104807.
6. Broms, B.B. (1964) Lateral resistance of piles in cohesionless Soils. Journal of Soil Mechanics and Foundation Engineering Division, ASCE 90, SM-3, p.123-1564.
7. Carvalho, D.; Albuquerque, P.J.R.; Claro, A.T.; Ferreira, C.V. (1996) Analysis of a pile loaded transversely at the top in residual diabase soil. Proceedings of 3° Seminário de Engenharia de Fundações Especiais - S.E.F.E. III, São Paulo, 1996, Anais, Vol. 1, 145-154. (*in portuguese*)
8. Carvalho, D.; Albuquerque, P.J.R.; Giacheti, H.L. (2000) Experimental field for soil mechanics and foundations studies in Campinas. Proceedings of 4° Seminário de Engenharia de Fundações Especiais - S.E.F.E. IV, São Paulo, 2000, Anais, Vol.3, 79-87. (*in portuguese*)
9. Davisson, M. T. (1970) Lateral load capacity of piles. Highway Research Record, n. 333, Pile Foundations, National Research Council, Washington, D.C., p.104-112.
10. Davisson, M.T.; Gill, H.L. (1963) Laterally loaded piles in a layered soil system. Journal of the Soil Mechanics and Foundation Division, ASCE, vol. 89, SM-3, p.63-94.
11. Dudley, J.H. (1970) Review of Collapsing Soils. Journal of the Soil Mechanics and Foundation Division. ASCE, Vol. 96, n. SM3, 925-947.
12. García, F.J.A., Cunha, R.P., Albuquerque, P.J.R.; Farias, M.M.; Bernardes, H.C. (2023) Experimental and Numerical Behavior of Horizontally Loaded Piled Rafts with a Defective Pile. Geotech Geol Eng 41, 429–439. https://doi.org/10.1007/s10706-022-02288-2
13. Jennings, J.E.; Knight, K. (1957) The Additional Settlement of Foundations Due to a Collapse of Structure of Sandy Sub Soils on Wetting. Proceedings of IV International Conference on Soil Mechanics And Foundation Engineering. Proceedings. Vol.1, London, 316-319.
14. Kassouf, R., Carvalho, D.; Albuquerque, P. J. R. (2016) The behavior of a foundation transversally loaded at the top over highly porous and collapsible soil DYNA 83 (199) pp. 134-139, https://doi.org/10.15446/dyna.v83n199.52529.

15. Matlock, H.; Reese, L.C. (1960). Generalized solutions for laterally loaded piles. Journal of Soil Mechanics and Foundation Engineering Division - ASCE, 86 (SM5), p. 63-91.
16. Matlock, H.; Reese, L.C. (1961) Foundation analysis of offshore pile supported structures. Proceedings of International Conference on Soil Mechanics and Geotechnical Engineering, 5, v. 2, p. 91-97.
17. Matlock, H.; Reese, L.C. (1961) Generalized solutions for laterally loaded piles. Journal of the Soil Mechanics and Foundation division, ASCE, Vol.86, SM5, 63-91.
18. Miche, R.J. (1930) Investigation of piles subjected to horizontal forcer. Application to quay walls. Journal of the School of Engineering, n. 4, Giza, Egipt.
19. Palmer, L.A.; Thompson, J.B. (1948) The Earth pressure and deflection along the embedded lengths of piles subject to lateral thrusts". Proceedings of 2nd International Conferences on Soil Mechanics and Foundation Engineering. Rotterdam, vol.5, p.156-161.
20. Poulos, H.G. (1971) Behavior of laterally loaded piles: I – Single Piles. Journal of the Soil Mechanics and Foundation Engineering Division, ASCE 9795, p.711-731.
21. Poulos, H.G.; David, E.H. (1980) Pile Foundation analysis and Design. John Wiley and Sons, New York, USA, 357p.
22. Rosendo, D.C.; Albuquerque, P.J.R. (2021) General analytical solution for laterally loaded pile based Miche model. Geotech Geol Eng 39, 765–782. https://doi.org/10.1007/s10706-020-01520-1
23. Terzaghi, K. (1955) Evaluation of coefficients of subgrade reaction. Géotechnique, 5 (4), p. 297-326.
24. Vargas, M (1978) Introduction to soil mechanics. McGraw-Hill do Brasil, Editora da Universidade de São Paulo, São Paulo, 509p. (*in portuguese*)

This page is intentionally left blank

Scan to know paper details and
author's profile

Comparison of Thermal Numerical Simulation Data with Experimental Data From the ISCT 200-US Permanent Magnet Hall Thruster

Marconi C. Porto, Alexandre A. Martins, José Leonardo Ferreira & Carlos Humberto Llanos

University of Brasilia

ABSTRACT

Due to its great efficiency, the Plasma Physics Laboratory of the Physics Institute of the University of Brasilia (PPL/PI/UnB) has been developing Hall thrusters since 2004. Testing NeFe and SmCo permanent magnets, excellent results were achieved with the PHALL II series (PPL). However, permanent magnets have limitations due to the working temperature (determined by the Curie temperature). Therefore, it is necessary to strictly control its temperature to avoid the demagnetization effect.

In this work, the results of the numerical thermal simulation were compared with experimental temperature results for the ISCT200-US Hall Thruster in order to verify the reliability of the simulation tool, allowing its future use in simulations of other Hall thrusters. Experimental temperature values and, whenever possible, dimensions and materials of the propellant components were collected from references on the ISCT200-US. A mechanical drawing of the ISCT 200-US was created, a numerical thermal simulation was developed, temperature simulation values were collected and compared with experimental values.

Keywords: hall thruster electric propulsion thermal numerical simulation ISCT 200-US thermal dissipation aerospace.

Classification: LCC Code: TL787-TL4050

Language: English

Great Britain Journals Press

LJP Copyright ID: 392922
Print ISSN: 2631-8474
Online ISSN: 2631-8482

London Journal of Engineering Research

Volume 23 | Issue 5 | Compilation 1.0

Comparison of Thermal Numerical Simulation Data with Experimental Data From the ISCT 200-US Permanent Magnet Hall Thruster

Marconi C. Porto[α], Alexandre A. Martins[σ], José Leonardo Ferreira[ρ]
& Carlos Humberto Llanos[Ѡ]

ABSTRACT

Due to its great efficiency, the Plasma Physics Laboratory of the Physics Institute of the University of Brasilia (PPL/PI/UnB) has been developing Hall thrusters since 2004. Testing NeFe and SmCo permanent magnets, excellent results were achieved with the PHALL II series (PPL). However, permanent magnets have limitations due to the working temperature (determined by the Curie temperature). Therefore, it is necessary to strictly control its temperature to avoid the demagnetization effect.

In this work, the results of the numerical thermal simulation were compared with experimental temperature results for the ISCT200-US Hall Thruster in order to verify the reliability of the simulation tool, allowing its future use in simulations of other Hall thrusters. Experimental temperature values and, whenever possible, dimensions and materials of the propellant components were collected from references on the ISCT200-US. A mechanical drawing of the ISCT 200-US was created, a numerical thermal simulation was developed, temperature simulation values were collected and compared with experimental values. A coherent comparison was achieved, which demonstrated the reliability of the simulation tool. Such results are important for the space qualification of thrusters subsequent to the PHALL II series.

Keywords: hall thruster electric propulsion thermal numerical simulation ISCT 200-US thermal dissipation aerospace.

Author α σ ρ: Plasma Physics Laboratory, Physics Institute, University of Brasilia, Brasilia, Brazil.

α Ѡ: Embedded Systems and Integrated Circuit Applications Laboratory, Mechanical Engineering Department, University of Brasilia, Brasilia, Brazil.

I. INTRODUCTION

Hall thrusters are considered a type of electric thruster [1-6]. The main characteristic of an electric thruster is the ability to produce plasma by ionization of a neutral gas, by the inclusion of electric and magnetic fields in its medium, and generate impulse for its acceleration of the thruster. Normally used to correct the orbit and attitude of artificial satellites and the propulsion of space probes, the Hall thruster has as its basic shape a cylindrical channel, an anode at the bottom of this channel, a magnetic field inside the channel and an external cathode [6]. Its operation consists of injecting a neutral gas into the channel, emitting electrons from the cathode towards the anode; the thruster then confines the electrons in an ExB Hall current that creates a virtual cathode above the anode. In this way, the electric field between the anode and the virtual cathode accelerates the ions out of the channel, generating thrust. The first flight tests of the Hall thruster took place in the 1960s [1,5–7].

The Physics Laboratory of the Physics Institute of the University of Brasília (PPL/PI/UnB) has been developing Hall Thrusters since 2004 [1,2,8,9] under the name PHALL Project. It is an incremental project, having started with PHALL I, followed by PHALL II-A, PHALL II-B and currently the PHALL II-C version (Fig. 1 and 2). The current version has a TRL 3 classification (Technology Readiness Level, NASA). The next, more compact and efficient version, to be developed by PPL, supported by the Brazilian

Space Agency (AEB), is the PHALL III [1] to reach TRL 6. The ultimate objective is to develop a Hall thruster for micro and small aritifical satellites fully qualified for spaceflight with TRL 9 classification. Other PPL work includes an HPT thruster (Fig. 3) in different versions, elimination of biological contaminants using plasmas and deposition of thin carbon films.

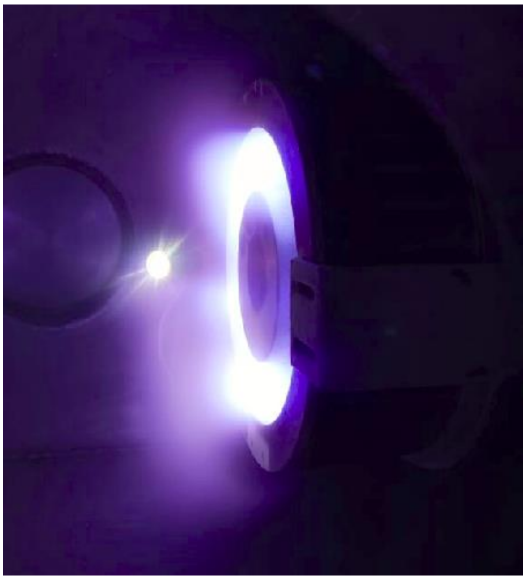

Fig. 1: Side View of PHALL II-C in Operation (PPL/PI/UnB)

The present work aims to verify the reliability of a thermal numerical simulation strategy and corroborate the results obtained in a similar work carried out by PPL with the BPT-4000 thruster [11]. Such confirmation will allow future tests with PHALL III and its subsequent versions.

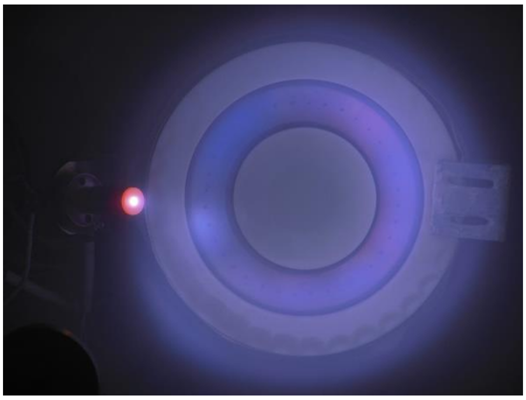

Fig. 2: Front view of PHALL II-C in operation (PPL/PI/UnB)

A systematic bibliographic research was carried out to find articles in which Hall thruster experiments with sufficient data to perform a simulation were presented. No studies were found that compared results from experiments and thermal simulations. Thus, the main advantage of the results of this study in relation to other experimental and thermal simulation studies is the fact that they indicate good reliability for commercial simulation software widely used in relation to thermal simulations of Hall Thrusters. In this research, few options were found, two of which were advantageous for developing work like this: one option was the Hall BPT4000 thruster (discharge power of 4500 W, electromagnetic coils), the study of which was developed by PPL in [11]; and the other option was the Hall ISCT200-US thruster (200 W discharge power, permanent magnets), the study of which is developed in the present work. The study carried out proposes to carry out a study that presents a good approximation between the contexts of the PHALL II-C and ISCT200-US thrusters and not necessarily something extremely precise or exact to give direction to future work that approach thermal numerical simulations through the technique of finite elements.

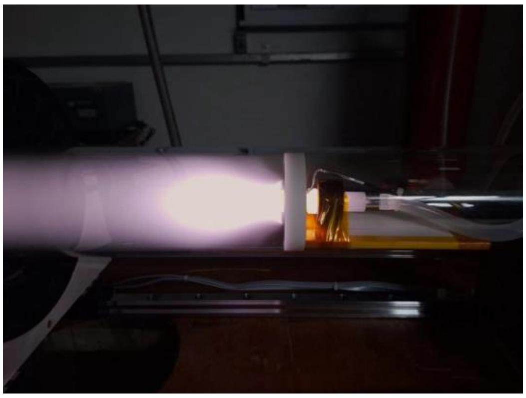

Fig. 3: HPT Thurster in Operation (PPL/PI/UnB)

The experimental data of the ISCT 200-US thruster [10] was collected from the literature and then thermal numerical simulation of this thruster was carried out. The simulation temperatures obtained were compared with the experimental ones, observing a good agreement with experimental data, with a small percentage difference. This fact indicates that this approach, based on finite elements, has good reliability on the Hall thruster simulation task, in addition to corroborating the results found in [11] for the BPT-4000 thruster.

Two software were considered to be used in the simulations, SolidWorks 2017 and Ansys 2017. Although a detailed benchmark was not performed, the Solid Works 2017 software proved to be the best option because the thermal model used by this software was found, but was not found for Ansys 2017 software. Additionally, SolidWorks 2017 has simpler CAD handling and is probably better known.

In future PPL work, supported by AEB, we will carry out an experiment to thermal study the PHALL III (next version) and, later, we will carry out a more precise comparison study with simulation software.

The main contributions of the present work are the following: (a) a verification of the reliability of a thermal numerical simulation of Hall thrusters (such a comparison between simulation and experiment was not found in the literature), (b) a verification of the equations for dissipated thermal powers in Hall thrusters (definition of an appropriate configuration of equations to support the system modeling problem using the finite element technique), (c) Corroboration of the results of this work with the results obtained in [11], with the exception that, this time, the thruster's magnetic field is generated by permanent magnets.

As a description of the sections of the article, we have: (a) section 2, which describes the methodology, (b) section 3, which presents the mathematical models, (c) section 4, with the results and their analysis, and (d) section 5, presenting the most relevant conclusions.

II.METHODOLOGY

Below is, in summary form (with greater detail in the subsections), the procedure adopted.

a) From reference [10], the experimental temperatures of the ISCT 200-US thruster were collected.
b) The thermal power dissipated generated by the thruster was calculated.
c) The materials for the ISCT 200-US components were selected.
d) The 3D CAD mechanical drawing was copied from the references.
e) Simulated and experimental temperature data were compared.

2.1 Experimental Temperatures

From Ref. [10], the average experimental temperatures were consulted in the following parts of the thruster: anode, internal wall and external wall (blue in Fig. 4).

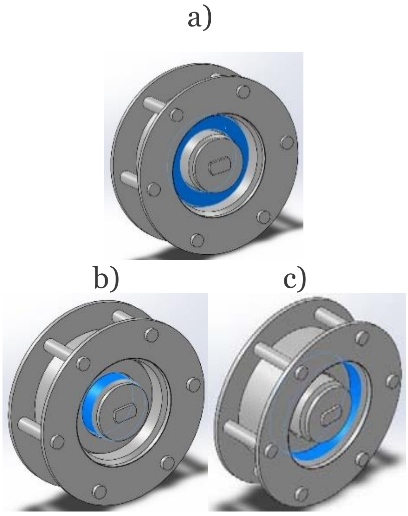

Fig. 4: Regions (in blue) of the ISCT200-US Where Experimental Temperatures Were Measured: (A) Anode, (b) Inner Wall, and (c) Outer Wall

Such temperatures are given in Table 1. No data were found in the literature on thermal contact resistances related to ISCT 200-US. Another way to obtain this data would be through temperature measurement in experiments on a real physical model, which was not viable. Therefore, thermal contact resistances were disregarded in the simulation.

Table 1: Average Experimental Temperatures of the ISCT 200US

ISCT200-US	Anode (°C)	Inner Wall (°C)	Outer Wall (°C)
Experiment	440.00	420.00	413.00

2.2 Dissipated Termal Powers

The following steps were followed in order to determine the dissipated thermal powers used in the ISCT 200-US simulation: some internal experimental data from PHALL II-C (such as, for example, plasma potential, floating potential and electron density) were used in the model for thermal energy dissipation [6,12] to calculate the power dissipated in PHALL II-C. After that, using the power dissipated in the PHALL IIC, the power dissipated in the ISCT 200-US was calculated proportionally to the discharge power of the PHALL II-C (subsection 3.1).

2.3 ISCT 200-US materials and mechanical drawing

With the help of information found in works [10,14,15,17], the mechanical drawing in 3D CAD was generated. Fig. 5 shows the exploded view of the mechanical drawing. Because they have little influence on heating and to speed up the simulation process, the fasteners were omitted. Fig. 6 shows a perspective view of the assembled thruster. In Table 2, you can find the main measurements of the mechanical drawing of the ISCT200-US compared to the measurements of the PHALL II-C. And in Fig. 7, there is a perspective view of PHALL II-C.

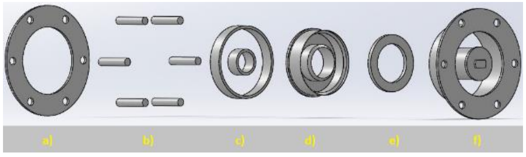

Fig. 5: Exploded View of the Mechanical Drawing of the ISCT200-US Thruster. From Left to Right: (a) Base Piece, (b) 6 Tubes for Heat Transmission, (c) Representation of Permanent Magnets, (d) Ceramics, (e) Anode, and (f) Structure

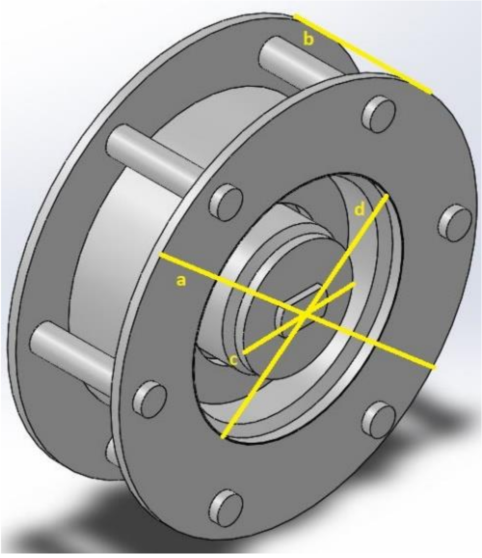

Fig. 6: Perspective View of the Mechanical Drawing of the ISCT200-US Thruster

The materials were consulted in works [10,14-17] related to the ISCT 200-US thruster, as far as possible. When there was not enough information, the same materials (or similar materials) as the PHALL II-C thruster were used. The materials used in the simulation are presented with the relevant physical properties in Table 3.

Table 2: Main measurements of the Mechanical Drawing for the Simulation of the ISCT200-US (Figure 6) and the PHALL II-C (Figure 7)

Part of the Thruster	Values (mm)	
	ISCT200-US	PHALL II-C
Front View Diameter	85.00 (a)	151.40 (e)
Length	26.50 (b)	82.28 (f)
Discharge Channel Internal Diameter	26.00 (c)	68.01 (g)
Discharge Channel External Diameter	49.50 (d)	114.14 (h)

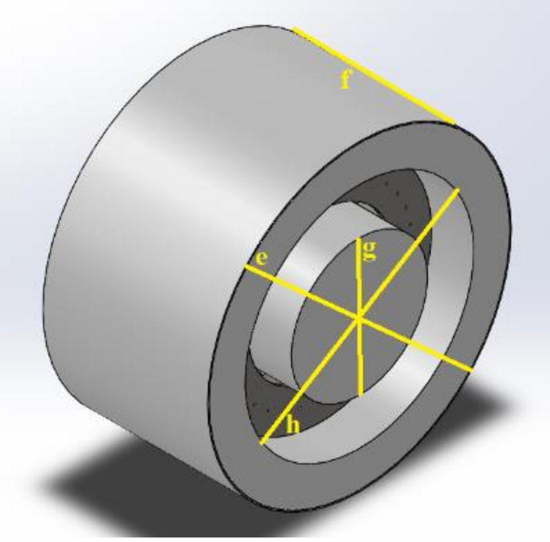

Fig. 7: Perspective View of the Mechanical Drawing of the PHALL II-C Thruster

Table 3: Materials of the ISCT200-US Components and Their Physical Properties

Component	Material	Mass Density (kg/m^3)	Thermal Conductivity (W/mK)	Specific Heat (J/kgK)	Emissivity
Structure	Stainless Steel 301	7880.00	21.40	500.00	0.59
Base Piece	Stainless Steel 301	7880.00	21.40	500.00	0.59
Anode	Stainless Steel 304 [16,17]	8000.00	16.20	500.00	0.19
Ceramics	BN-SiO$_2$ [10,14-17]	2100.00	11.00	770.00	0.90
Tubes	Copper [16,17]	8900.00	390.00	390.00	0.75
Permanent magnets	Sm$_2$Co$_{17}$ [16,17]	8400.00	11.63	376.81	0.11

III. MATHEMATICAL MODELS

3.1 Model for Thermal Energy Dissipation

The dissipated thermal power values used for the ISCT200-US thruster simulation were calculated proportionally to the same values for the PHALL II-C thruster. To calculate the dissipated thermal powers of the PHALL II-C, a model for thermal energy dissipation in Hall thrusters [6,12] was used, into which the thruster thruster plasma data can be inserted. The equation for the discharge power P_d [12] is:

$$P_d = P_b + P_w + P_a + P_r + P_{ions}, \tag{1}$$

where P_b is the beam power, P_w is the power dissipated in the walls, P_a is the power dissipated in the anode, P_r is the radiative power loss from the plasma, and P_{ions} is the power to produce ions.

The beam power is defined by the equation:

$$P_b = V_b I_b, \tag{2}$$

where V_b is the beam voltage, I_b is the beam current. The following equation is the power dissipated in the walls:

$$P_w = n_e e A_w \left[\left(\frac{kT_e}{e}\right)^{\frac{3}{2}} \left(\frac{2e}{\pi m}\right)^{\frac{1}{2}} e^{\frac{e\phi_S}{kT_e}} + \frac{1}{2}\left(\frac{kT_e}{M}\right)^{\frac{1}{2}} (\varepsilon - \phi_S) \right], \tag{3}$$

where n_e is the electronic density, e is the electron charge with positive value, A_w is the surface area of the wall in contact with the plasma, k is the Boltzmann constant, T_e is the temperature electronic in Kelvins, m is the electron mass, ϕ_S is the sheath potential relative to the plasma ($-V_f$), M is the mas of the Argon atom (PHALL II-C propellant), and ε is the pre-sheath ion energy. The power dissipated in the anode can be calculated by the following equation:

$$P_a = 2T_{eV}I_a \approx 2T_{eV}I_d, \tag{4}$$

where T_{eV} is the electronic temperature in electron-volts, I_a is the anode current, and I_d is the discharge current. The following equation represents the radiative power loss from the plasma:

$$P_r = n_o n_e \langle \sigma * v_e \rangle V_{pr}, \tag{5}$$

where n_o is the neutral density, $<\sigma^* v_e>$ is the excitation rate coefficient that includes the excitation cross-section and the electron velocity, and V_{pr} is the volume of the high temperature plasma region. For the power to produce ions, we have the following equation:

$$P_{ions} = (I_b + I_{iw})U^+, \tag{6}$$

where I_{iw} is the ionic current to the wall, and U^+ ionization potential. The following equation was used for the pre-sheath ion energy [6]:

$$\varepsilon = 0.58\frac{kT_e}{e}. \tag{7}$$

The equations effectively used to calculate the dissipated thermal powers in the walls and in the anode (parts in contact with the plasma) were equations (3), (4) and (7). First, the total dissipated thermal power in the walls and the dissipated thermal power in the anode were calculated for the PHALL II-C, both for the discharge power of 195.00W and for 470.53W. The values of the parameters used in the equations can be found in Table 4 (in the case of the values measured experimentally) and in Table 5, while the values of the calculated powers can be found in Table 6. The values obtained experimentally are internal experimental data and were measured using a Langmuir probe, whose tip was placed in the plasma plume 20cm from the PHALL II-C thruster.

From Table 4, V_p is the plasma potential, V_f is the floating potential, T_{eV} is the electron temperature in electron-volts, and n_e is the electron density.

Table 4: Average Data for PHALL II-C Performance

Parameters	Discharge Power 195.00W (Anode: 78.00V, 2.50A)	Discharge Power 470.53W (Anode: 105.50V, 4.46A)
$V_p\,(V)$	77.00	104.00
$V_f\,(V)$	8.00	10.00
$T_{eV}\,(eV)$	4.28	5.61
$n_e\,(m^{-3})$	2.06×10^{16}	2.13×10^{16}

Table 5: Data for PHALL II-C

Parameters	Discharge Power 195.00W (Anode: 78.00V, 2.50A)	Discharge Power 470.53W (Anode: 105.50V, 4.46A)
$T_e\,(K)$	49667.26	65101.25
$I_d\,(A)$	2.50	4.46
$e\,(C)$	1.60×10^{19}	1.60×10^{19}
$A_w\,(m2)$	3.76×10^{-3}	3.76×10^{-3}
$k\,(J/K)$	1.38×10^{-23}	1.38×10^{-23}
$m\,(kg)$	9.11×10^{-31}	9.11×10^{-31}
$M\,(kg)$	6.63×10^{-26}	6.63×10^{-26}
$\phi_S\,(V)$	-8.00	-10.00
$\varepsilon\,(V)$	2.48	3.25

Then, the ratios for walls, equation (8), and anode, equation (9), between the values of dissipated thermal power and discharge power were calculated for both the 195.00W case and the 470.53W case. After that, the average between the two cases was calculated (Table 7). The ratio equations are shown below:

$$R_w = \frac{P_w}{P_d}, \tag{8}$$

$$R_a = \frac{P_a}{P_d}. \tag{9}$$

Where R_w is the ratio for walls, P_w is the power dissipated in the walls, P_d is the discharge power, R_a is the ratio for anode and P_a is the power dissipated in the anode.

These ratios calculated for the walls and for the anode were used to calculate, proportionally to the discharge power of the ISCT200-US, the total dissipated thermal power in the walls and the dissipated thermal power in the anode (Table 8). After that, the dissipated thermal powers in each particular wall were calculated.

Table 6: Dissipated Thermal Powers of walls and anode for PHALL II-C

Part of the PHALL II-C	For Disch. Power 195.00W	For Disch. Power 470.53W
Walls	58.89W	99.24W
Anode	21.40W	50.04W

We have that in [18] the depositions of thermal energy in the anode in the radial direction and in the internal and external walls of the discharge channel in the axial direction are practically constant, as we put in the simulation of the ISCT200-US; already the reference [19] indicates an almost constant temperature distribution in the anode and with a small variation in the internal walls (approximately from 910K to 1090K) and external (approximately from 910K to 1080K) of the discharge channel, which corroborates with the distribution of thermal energy deposition in [18]

Table 7: Ratios Between the Values of Dissipated Thermal Power and Discharge Power for PHALL II-C

Part of the PHALL II-C	For Disch. Power 195.00W	For Disch. Power 470.53W	Average
Walls	0.3020	0.2109	0.2565
Anode	0.1097	0.1064	0.1081

We need the value on each wall for the simulations. The total thermal power dissipated in the walls is the sum of the powers in each wall – see equation (8). The power division used by us was determined by analyzing [13], where the inner wall of the discharge channel heats up more than the outer wall. According to [13], the temperature of the inner wall is higher than the temperature (550K-600K) of the outer wall of the T-140 HET (Hall thruster) for a discharge power of 630W (the smallest in the study carried out in [13] and the closest to the discharge power of the ISCT200-US). Furthermore, where we have to include analysis of the relationship between the surface areas of the inner and outer walls.

Table 8: Dissipated Thermal Powers of Walls and Anode for ISCT200-US

Part of the PHALL II-C	Dissip. Thermal Power (W)
Walls	51.29
Anode	21.61

Such a relationship shows that the area of the inner wall of the PHALL II-C is approximately 60% of the area of its outer wall (the division of the area of the inner wall by the area of the outer wall is equal to 0.5958). This is an indication that the dissipated thermal power per unit area (power density) is almost twice as high in the inner wall. Considering also that the magnetic field is stronger at the inner wall, it is expected that it will be subject to more plasma impact along magnetic field lines than the outer wall.

Because of this, a power density (power/area) ratio between the inner and outer walls of about 2:1 is expected, which is the value required to obtain a temperature difference between the inner and outer walls similar to that shown in [13].

For the center and edge walls, located in front of the thruster (Figure 3), the proportion of power density was considered equal to that of the inner wall, due to the deposition shown in PHALL II-C thruster, where the experimental data of plasma was collected. Equations (10) to (12) below were used to calculate the powers in each wall:

$$P_{wB} = P_o + P_i + P_c + P_e \tag{10}$$

$$n\frac{P_o}{A_o} = \frac{P_i}{A_i} = \frac{P_c}{A_c} = \frac{P_e}{A_e} \tag{11}$$

$$n = 2 \tag{12}$$

where P is the power in a given wall, A is the area of a given wall, the subscripts o, i, c, e refer, respectively, to the outer wall, inner wall, center wall and edge wall, with n being a factor of proportionality. The blue regions in Figure 6 indicate where the P_o, P_i, P_c e P_e powers are applied to the respective surfaces.

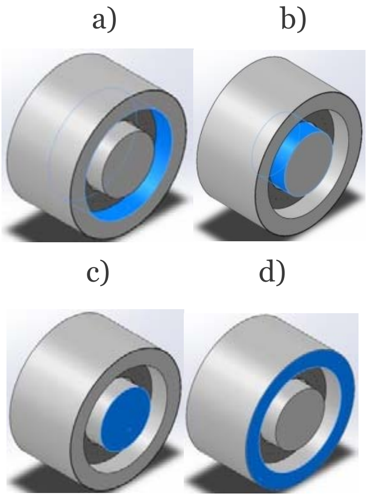

Fig. 8: Identification (blue color) of the wall surfaces considered for local power deposition in the PHALL II-C thruster: (a) outer wall, P_o, (b), inner wall, P_i, (c) central wall, P_c and (d) edge wall, P_e

For a discharge power of 200 W, the dissipated thermal powers for each part of the ISCT200-US are found in Table 9.

Table 9: Dissipated thermal powers for the ISCT200-US thruster

Part of the ISCT200-US	Power (W)
Anode	21.61
Inner Wall	9.25
Outer Wall	8.17
Central Wall	4.49
Edge Wall	29.38

3.2 The Thermal Model

The thermal model was determined from the theoretical manual [20] of the commercial software used (SolidWorks 2017, from the manufacturer Dassault Systemes). For simulation calculations, the geometry of the solid that forms the thruster is divided into smaller parts - called finite elements (Figure 9); In this way, the structure of the solid becomes a discrete system with a set of discrete equations for the thermal model:

$$[C_T]\left[\frac{\partial T}{\partial t}\right] + [K]\{T\} = \{R\}. \qquad (13)$$

Fig. 9: Mechanical Drawing of the ISCT200-US Thruster With the Subdivision of the Solid Into Finite Elements

In this case, T is the temperature at the element and is given by:

$$T = [D]\{T_n\}, \qquad (14)$$

where *[D]* is a vector of shape or interpolation functions (depends on the position of the element), *{Tn}* Is a column vector of nodal temperatures and possible temperature derivatives. *[C_T]* is calculated by equation (15).

$$[C_T] = \iiint_{\Delta V} \rho\, c [D]^T [D] dV, \qquad (15)$$

where ΔV is the volume of the element, ρ is the mass density, and c is the specific heat. The other parameters are calculated according to equations (16) to (18)

$$[K] = [K_T], \qquad (16)$$

with

$$[K_T] = \iiint_{\Delta V} [B]^T\, [k][B] dV, \qquad (17)$$

$$[B] = \begin{Bmatrix} \frac{\partial D}{\partial x} \\ \frac{\partial D}{\partial y} \\ \frac{\partial D}{\partial z} \end{Bmatrix}. \qquad (18)$$

Futhermore,

$$\{R\} = \{R_Q\} - \{R_q\}, \qquad (19)$$

where *[k]* is the thermal conductivity and being

$$\{R_Q\} = \iiint_{\Delta V} Q\, [D]^T dV, \qquad (20)$$

where Q is the internally generated heat flux, and the last parameter, $\{R_q\}$ is calculated as shown in equation (21).

$$\{R_q\} = \iint_{\Delta Sq} q\, [D]^T dS, \qquad (21)$$

where ΔS_q is the boundary portion of the element and q is the boundary heat flux.

VI. RESULTS AND DISCUSSION

Starting with a simulation diagram of the ISCT200-US (Figure 10), the results obtained in the present work are presented below.

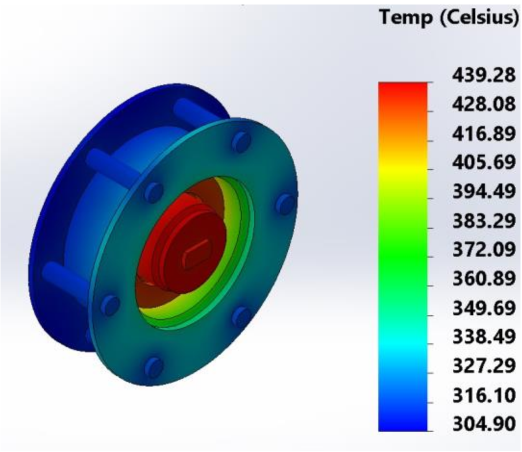

Fig. 10: ISCT200-US thruster simulation diagram

Regarding the three ISCT200-US regions considered in the experiment, the average temperatures achieved in the simulation and the experimental average temperatures presented in reference [10] are available in Table 10.

Table 10: Average Simulation Temperatures and Average Experimental Temperatures for the ISCT200-US Thruster

ISCT200-US	Anode (°C)	Inner Wall (°C)	Outer Wall (°C)
Experiment	440.00	420.00	413.00
Simulation	429.38	436.29	396.32
Difference	10.62	16.29	16.68
Percentage Difference	2.41%	3.88%	4.04%

The results obtained in the three regions considered (anode, internal wall and external wall) were very faithful to those presented by the experiments in reference [10], as a temperature difference (Table 10) between the experimental and simulated values was quite low, with an error (in percentage) having a variation between 2.41% and 4.04%.

It is estimated that the temperature difference between experimental and simulated data would be even smaller if the thermal contact resistances and all materials properly used in the ISCT200-US thruster were included in the simulation.

It is believed that the theoretical reliability of the equations for dissipated thermal power is reinforced due to the fact that they are used in the simulation to confirm the experimental data.

Due to the good results found, with the help of the equations, it appears that the simulation software is reliable.

Therefore, as the results indicate, future simulations of Hall thruster models with permanent magnets carried out using a tool based on finite elements will also be reliable for validation before obtaining experimental data.

These results also corroborate the developments in reference [11], in addition to providing greater precision. In reference [11], similar work was carried out with the BPT-4000 literature thruster.

V. CONCLUSIONS

A thermal numerical simulation of a Hall thruster found in the literature, called ISCT200-US, was carried out, in which the experimental data provided by the literature were compared with simulation results in order to verify the reliability of the simulation tool and the corroboration of the results with a work carried out with Hall BPT-4000 thruster. The difference between the experiment and simulation temperatures was small. The percentage of difference varied between 2.41% and 4.04%, which indicates that the simulation software and the approximations used present good reliability when applied to Hall thrusters, in addition to confirming the results found in [11] for the BPT-4000.

ACKNOWLEDGMENTS

Marconi C. Porto thanks CAPES for the support in the form of a Master's Degree Scholarship.

REFERENCES

1. J. L. Ferreira, A. A. Martins, R. A. Miranda, M. C. F. Porto, H. O. Coelho, Hall plasma thruster devlopment for micro and nano satellites, J. Phys.: Conf. Ser. 1365 012026 (2019).
2. J. L. Ferreira, A. A. Martins, R. A. Miranda, A. Schelling, L. S. Alves, E. G. Costa, H. O. Coelho, A. C. Branco, F. N. O. Lopes, Permanent magnet Hall thruster development and applications on future brazilian space missions, J. Phys.: Conf. Ser. 641 012016 (2015).
3. S. Reilly, M. Sekerak, R. Hofer, Transient Thermal Analisys of the 12.5 kW Hermes Hall Thruster, 52nd AIAA/SAE/ASEE Joint Prop. Conf. AIAA 2016-5024 (2016).
4. N. Turan, U. Kokal, M. Celik, H. Kurt, Experimental Study of the Effects of the Cathode Position and the Electrical Circuit Configuration on the operation Hall Thruster Bustlab Hollow Cathode, 52nd AIAA/SAE/ASEE Joint Prop. Conf. AIAA 2016-4834 (2016).
5. R. W. Conversano, Low-Power Magneticaly Shielded Hall Thrusters, PhD Thesis, University of California. (2015).
6. D. M. Goebel, I. Katz, Fundamentals of Electrical Propulsion, John Wiley. (2008).
7. R. W. Conversano, R. B. Lobbia, K. C. Tilley, D. M. Goebel, S. W. Reilley, I. G. Mikellides, R. R. Hofer, Development and Initial Performance Testing of a LowPower Magnetically Shielded Hall Thruster with an Internally-Mounted Hollow Cathode, 35th Int. Elec. Prop. Conf. IEPC-2017-64 (2017).
8. A. A. Martins, M. C. F. Porto, H. O. Coelho, J. L. Ferreira, I. S. Ferreira, Preliminary experimental results of the PHALL II-C with improved magnetic circuit design and hollow cathode, J. Phys.: Conf. Ser. 1365 012025 (2019).
9. R. A. Miranda, A. A. Martins, J. L. Ferreira, Particle-in-cell numerical simulations of a cylindrical Hall thruster with permanent magnets, J. Phys.: Conf. Ser. 911 02021 (2017).
10. L. Grimaud, S. Mazouffre, Ion behavior in low-power magnetically shielded and unshielded Hall thrusters, Plasma Sources Sci. Technol. 26 (2017) 055020.
11. M. C. Porto, A. A. Martins, J. L. Ferreira, C. H. Llanos, Comparative analysis of simulation and experiment for the Hall-type thruster BPT-4000, Results in Engineering, 17 (2023) 101006.
12. R. W. Conversano, D. M. Goebel, R. R. Hofer, T. S. Matlock, R. E. Wirz Magnetically Shielded Miniature Hall Thruster: Development and Initial Testing, 33rd Int. Elec. Prop. Conf. IEPC-2013-201 (2013).
13. R. A. Martinez, H. Dao, M. L. R. Walker, Power deposition into the discharge channel of a hall effect thruster, Journal of Propulsion and Power. (2014) Vol. 30, No. 1, 209220, DOI: 10.2514/1.B34897.
14. L. Grimaud, S. Mazouffre, Performance comparision between standard and magnetically shielded 200 W Hall thrusters with BN-SiO$_2$ and graphite channel walls, 35th Int. Elec. Prop. Conf. IEPC-2017-127 (2017).
15. L. Grimaud, S. Mazouffre, Conducting wall Hall thrusters in magnetic shielding and standard configurations, Journal of Applied Physics 122, 033305 (2017).
16. S. Mazouffre, L. Grimaud, S. Tsikata, K. Matyash, R Scheinder, Investigation of rotating spoke instabilities in a wall-less Hall thruster. Part I: Experiments, 35th Int. Elec. Prop. Conf. IEPC-2017-248 (2017).

17. A. Spethmann, T. Trottenberg, H. Kersten, F. G. Hey, L. Grimaud, S. Mazouffre, Application of force measuring probes for the investigation of sputtering and as diagnostic for HEMP and Hall thrusters, 35th Int. Elec. Prop. Conf. IEPC-2017-245 (2017).
18. L. Yan, P. Wang, H. Ouyang, X Kang. Thermal analisys of the Hall Thruster in vacuum, Vacuum. (2014) Vol. 108, 40-55.
19. R. A. Martinez, M. R. L. Walker, Propellant thermal management effect on neutral residence time in low-voltage Hall thrusters, Journal of Propulsion and Power. (2013) Vol. 29, No. 3 528-539, DOI: 10.2514/1.B34702.
20. Dassault Systemes, Theoretical Manual for SolidWorks. (2017).

This page is intentionally left blank

Scan to know paper details and
author's profile

The Usage of Wireless Intelligent Control and UAV-Enabled B5G/6G Network in Fuzzy Adaptive Kalman Filter in INS/GNS Integrated Navigation System

Guangchen Xu & Zhenliang Yu

ABSTRACT

In the Inertial Navigation System/Geomagnetic Navigation System (INS/GNS) integrated navigation system, divergence and measurement noise that change with environments frequently occur must be reduced so as to extend the accuracy and stability of autonomous, passive navigation. Base on the Unscented Kalman Filter, we can combine Convergence of intelligent sensing as well as computing, and control for UAV-enabled B5G/6G network to deal with change in the variance and mean value of the late- st information. First, the noise's covariance in the model is modified "online" to change the estimation of mean square deviation error and filtering gain of Kalman filtering by using 5G/6G network; Then, through UAV-enabled B5G/6G network and intelligent sensing to change the scaling factor of weight in sigma sampling is adaptively changed to solve the nonlocal effect in UT transform and improve the effciency and accuracy of the navigation deposition system. The simulation findings reveal that the fuzzy adaptive Kalman filter is very efficient for INS/GNS integrated navigation systems. It overcome the short comings of traditional filtering method and improve rove the accuracy of filtering.

Keywords: fuzzy adaptive; integrated navigation; scaling factor; unscented kalman filter; ut transform; B5G/6G.

Classification: LCC Code: QA75.5-QA76.95

Language: English

Great Britain Journals Press

LJP Copyright ID: 392923
Print ISSN: 2631-8474
Online ISSN: 2631-8482

London Journal of Engineering Research

Volume 23 | Issue 5 | Compilation 1.0

The Usage of Wireless Intelligent Control and UAV-Enabled B5G/6G Network in Fuzzy Adaptive Kalman Filter in INS/GNS Integrated Navigation System

Guangchen Xu[α] & Zhenliang Yu[σ]

ABSTRACT

In the Inertial Navigation System/Geomagnetic Navigation System (INS/GNS) integrated navigation system, divergence and measurement noise that change with environments frequently occur must be reduced so as to extend the accuracy and stability of autonomous, passive navigation. Base on the Unscented Kalman Filter, we can combine Convergence of intelligent sensing as well as computing, and control for UAV-enabled B5G/6G network to deal with change in the variance and mean value of the latest information. First, the noise's covariance in the model is modified "online" to change the estimation of mean square deviation error and filtering gain of Kalman filtering by using 5G/6G network; Then, through UAV-enabled B5G/6G network and intelligent sensing to change the scaling factor of weight in sigma sampling is adaptively changed to solve the nonlocal effect in UT transform and improve the effciency and accuracy of the navigation deposition system. The simulation findings reveal that the fuzzy adaptive Kalman filter is very efficient for INS/GNS integrated navigation systems. It overcome the short comings of traditional filtering method and improve rove the accuracy of filtering.

Keywords: fuzzy adaptive; integrated navigation; scaling factor; unscented kalman filter; ut transform; B5G/6G.

Author α σ: Mechanical and Power Engineering College, Yingkou Institute of Technology, Yingkou, China.

I. INTRODUCTION

The fundamental physical field of the Earth is the geomagnetic field. Any location in the vicinity of Earth has a magnetic field, and the strength and direction of the field depend on the location's longitude, latitude, and altitude. The geomagnetic field has abundant parameter information, such as the total geomagnetic field, the three-component geomagnetism, the inclination angle, the declination angle and the geomagnetic field gradient. This provides sufficient matching information for the geomagnetic navigation algorithm. Geomagnetic navigation does not need to receive external information and belongs to both active and passive navigation. The long-term stability of geomagnetic matching technology can make up for the deficiencies of the inertial navigation system's long-term faults if inertial navigation and geomagnetic matching technology are combined. Additionally, the geomagnetic matching system's vulnerability to interference can be offset by the inertial navigation system's short-term high precision. Inertial/geomagnetic integrated navigation can be applied to the autonomous navigation of submarines, ships, vehicles and other carriers as well as long-range weapons such as missiles.It has shown important military value and promising application prospects.

At present, geomagnetic navigation algorithms include the theory of maximum correlation, ICCP algorithm [1], neural networks and statistical pattern recognition algorithms, the most widely used of which is the extended Kalman filter (EKF) [2] method. In this method, the nonlinear system is linearized by the Taylor expansion method, and the linear transformation in the Kalman equation is replaced by the Jacobian matrix. Although EKF maintains the advantages of Kalman filtering and effective iterative updates in calculations, it essentially approximates linearization of nonlinear models. For strong nonlinear problems or when the Jacobian matrix is unavailable, the EKF cannot obtain satisfactory results [3].

Therefore, Julier and Uhlmann [4] put forward the Unscented Kalman Filter (UKF) method based on the idea of multiple function representative points, which overcomes the above shortcomings of EKF. However, in the practical application of UKF, obtaining statistical knowledge of system noise and observation noise is difficult. In general, the process noise, measurement noise and innovation are no longer white noise processes. In this case, traditional Kalman Filters can easily cause filtering to diverge. In this study, an adaptive Kalman filter is used to reduce the impact of unusual measurement data and produce precise system state estimate. The scaling factor α of the noise variance matrix in the model and the weight in the sigma sampling "on-line" can be changed to alter the estimated filter gain matrix and mean square error matrix.

II. METHODOLOGY

2.1 UT Transformation

The UT transformation serves as the cornerstone of UKF. The Unscented Transformation (UT) does not require linearization of the nonlinear system since a nonlinear probability distribution can be approximated more easily than any nonlinear function.Instead, it uses a certain sampling approach to choose a predetermined number of sigma sampling points. These sampling points have the same mean $\bar{x}$ and covariance P_{xx} as the system state distribution. After nonlinear transformation, these sigma sampling points can approach the posterior mean $\bar{y}$ and covariance P_{yy} with second-order accuracy. Applying the UT transform to the Kalman filter results in the UKF is formed. The following is the UT transformation process [5]:

According to the x statistics $\bar{x}$ and P_{xx} of the input variables, select a sigma point sampling strategy to obtain the sigma point set $\{\chi_i\}$, $i=1,\cdots L$ of the input variable and the corresponding weights W_i^m and W_i^c, where L is the number of sampling points used in the sampling strategy; The weights used for mean and covariance weighting are W_i^m and W_i^c, respectively.

Perform a nonlinear transformation on each sampling point in the sampled input variable sigma point set $\{\chi_i\}$ to obtain the transformed sigma point set $\{y_i\}$, $y_i = f(x_i), i=1,\cdots L$.

By weighting the sigma point set $\{y_i\}$ after nonlinear transformation, the statistics $\bar{y}$ and P_{yy} of the output variable y are obtained.

$$\bar{y} = \sum_{i=0}^{L-1} W_i^m y_i \tag{1}$$

$$P_{yy} = \sum_{i=0}^{L-1} W_i^c (y_i - \bar{y})(y_i - \bar{y})^T \tag{2}$$

2.2 Proportional Revision

The minimal skew simplex sampling is a strategy to minimize the number of sampling points. It minimizes the skewness (the third-order moment) on the premise that the sampling point set captures the first two order moments of the random variable x. In the minimum skewness simplex sampling strategy, the sampling points are not centrosymmetric. The nonlocal effect problem is caused by the fact that as the dimension grows, the distance from the sample point extending from the low dimension to the center point grows.Julier et al. proposed a proportional UT transform in which the sampling strategy in the general UT transform is proportionally modified [6]. This transformation can solve the problem of non-local effects by adjusting the value of the parameter α. The specific sigma point sampling rule is as follows:

$$\{\chi_i\} = [\bar{x} \quad \bar{x}+\sqrt{(L+\lambda)\ P_{xx}} \quad \bar{x}-\sqrt{(L+\lambda)\ P_{xx}}] \tag{3}$$

$$W_i^m = \begin{cases} \lambda/(L+\lambda), i=0 \\ 1/2(L+\lambda), i \neq 0 \end{cases} \tag{4}$$

$$W_i^c = \begin{cases} \lambda/(L+\lambda)+(1-\alpha^2+\beta), i=0 \\ 1/2(L+\lambda), i \neq 0 \end{cases} \tag{5}$$

Where $\lambda = \alpha^2(L+\kappa) - L$. Let be $\kappa \geq 0$ to ensure that the variance matrix is semidefinite, κ generally defaults to 0 or $3-L$. The scope of L is $0 < L < 3$. W_i^c and W_i^m are the weights used in the covariance and mean weighting of UT transform, respectively. α and β are parameters for the Gaussian distribution, $\beta = 2$ is optimal [7]. The distance between the sigma point and the center point $\bar{x}$ is managed by the scale factor α. It is a relatively small positive number, which is usually taken in the interval [$10^{-4} \sim 1$].

2.3 The Selection of Adaptive Scale Factor α

The flow of the UKF algorithm can be seen in Figure 1. The UKF filter value $\hat{X}_k$ at time k is taken as the center point of the sigma point set generated in the next time prediction, and the other sampling points are distributed near the center point.The covariance P_k matrix obtained by the k-step filtering describes the relationship between the filter value $\hat{X}_k$ and the real value X_k, namely:

$$P_k = E[(X_k - \hat{X}_k)(X_k - \hat{X}_k)^T] \tag{6}$$

Therefore, the distance d_k between the center point and the sigma point set can be approximately calculated by P_k, namely:

$$d_k \approx \sqrt{tr(P_k)} \tag{7}$$

The k-step filter value "approximately covers" the critical region $O(\hat{X}_k, d_k)$ of the true value, as the sampling range of the sigma sampling point in step k+1, calculates $d_{k+1} \approx \sqrt{tr(P_{k+1})}$, and obtains the adaptive adjustment measurement sigma sampling of scale factor $\alpha_{k+1|k}$ [8].

$$\alpha_{k+1|k} = d_k / d_{k+1} \tag{8}$$

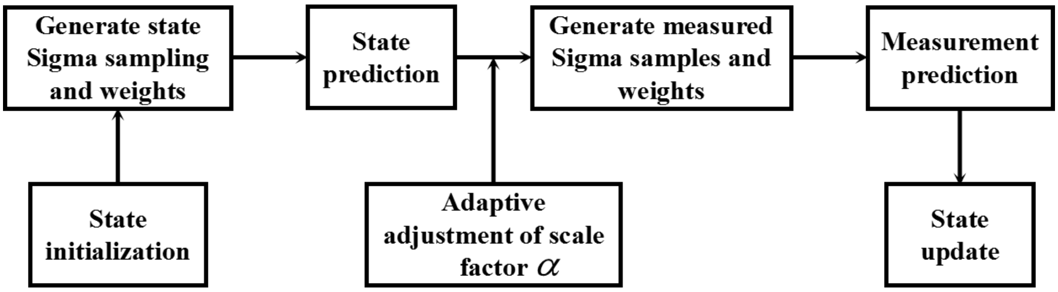

Figure 1: The flowchart of the Proportional Revision UKF Algorithm

2.4 Adaptive Control

The residual sequence in the Kalman filter should be white noise with a zero mean if the mathematical model is accurate enough. The Kalman filter's theoretical residual variance should be close to 1 when compared to the measured residual variance. Long-term deviations in the ratio show that the measurement noise level has changed, necessitating an adjustment to the noise covariance matrix sum [9]. To get the ratio back to close to 1, that is the standard for adjustment.

Let's set the model's noise variance matrix to:

$$\begin{cases} Q_k = \gamma Q \\ R_k = \gamma R \end{cases} \tag{9}$$

Where: Q is the system noise variance matrix, R is the measurement noise variance matrix. Matrices Q and R are fixed values; The adjustment value γ, modifies the measurement noise variance matrix and the system noise in an adaptive manner.The fuzzy adaptive Kalman filter is developed as follows to put the aforementioned idea into practice.

In the formula: the matrix sum is a fixed value. An adjustment value, adaptively adjusts the system noise and measures the noise variance matrix. The concepts discussed above are used to design the fuzzy adaptive Kalman filter[10].

The one-step prediction of the state estimate is:

$$\hat{X}_{k|k-1} = \Phi_{k,k-1}\hat{X}_{k-1} \qquad (10)$$

The n-dimensional state one-step transition matrix $\Phi_{k,k-1}$ is used in the equation.

The mean square error matrix of the one-step forecast is:

$$P_{k|k-1} = \Phi_{k,k-1}P_{k-1}\Phi^{T}{}_{k,k-1} + \gamma_k Q \qquad (11)$$

The Kalman filter's gain matrix is:

$$K_k = P_{k|k-1}H_k^T(H_k P_{k|k-1}H_k{}^T + \gamma_k R)^{-1} \qquad (12)$$

The measured value's one-step prediction is:

$$\hat{Z}_k = H_k\hat{X}_{k|k-1} \qquad (13)$$

Then, the estimated modified state is:

$$\hat{X}_k = \hat{X}_{k|k-1} + K_k(Z_k - \hat{Z}_k) \qquad (14)$$

In addition to least, the matrix of posterior mean square errors is:

$$P_k = (I - K_k H_k)P_{k|k-1} \qquad (15)$$

The $r = Z_k - \hat{Z}_k$, also known as residual or innovation, measures how dependent the system model is on the measured values. Where, I represents the identity matrix, whose dimension is the same as the system status quantity [11].

2.5 The Fuzzy Adjustment

Fuzzification, the creation of fuzzy control rules, and defuzzification are the three steps in the fuzzy calculation process. The output fuzzy quantity is produced by the fuzzy control rules by inferring from the input fuzzy quantity. The input exact quantity is converted to the input fuzzy quantity using fuzzyification. [12]. The output fuzzy quantity is converted into the precise quantity output during the final defuzzification procedure.

The mean value $\bar{r}$ and variance $\hat{P}_r$ of the innovation are the inputs to the fuzzy adaptive logic system employed in this study, and the output is a weighted index that is used to modify the noise variance matrix in the system model.

Ideally, the innovation is zero-mean white noise. If the innovation is not zero-mean white noise in the process of system operation, it indicates that there is a problem with the filter. Assuming that it represents statistics n over a period of time, the mean and variance of innovation are:

$$\bar{r} = \frac{1}{n}\sum_{j=t-L}^{t} r_j \qquad (16)$$

$$\hat{P}_r = \frac{1}{n}\sum_{j=t-L+1}^{t} r_j r_j{}^T \qquad (17)$$

Compare the theoretical value of the variance to the estimated value of the variance. When the estimated value becomes larger than the theoretical value and the mean value gradually moves away from the zero point, it indicates that the filter becomes more and more unstable. At this moment, adjusting the noise intensity is required to enhance the filter's performance.

The mean and variance are determined by keeping track of the innovation at each filter sample point. If the variance of innovation increases and the mean value approaches zero, the system noise should be reduced while the measurement noise should be increased to obtain a smaller γ value. As a result, the gain matrix of the filter will diminish the system's trust and use of the measured value and the filtering performance tends to become more stable.

The innovation variance and mean value are divided into three levels as fuzzy input: Zero, Small, and Large; The output γ is divided into four levels: Zero, Small, Medium, and Large; The common method of generating fuzzy control rules is through expert experience, expressed in the form shown in Table 1.

Table 1: Rules for fuzzy inference

γ		Mean $\bar{r}$		
		Zero	Small	Large
Variance $\hat{P}_r$	Zero	Large	Zero	Large
	Small	Zero	Large	Medium
	Large	Large	Medium	Zero

2.6 The Proportional Minimum Skewness UKF Algorithm of Fuzzy Adaptive

Following linearization, the discrete system's mathematical model looks like this:

$$\begin{cases} X_k = \Phi_{k,k-1} X_{k-1} + \omega_k \\ Z_k = H_k X_k + \upsilon_k \end{cases} \tag{18}$$

X_k, Z_k, and H_k represent the system state vector, measurement vector, and measurement matrix, respectively. The system noise vector ω_k is white noise, namely: $\omega_k \sim N(0,Q)$, Q is the system noise variance matrix; The measurement noise vector υ_k is also white noise, namely: $\upsilon_k \sim N(0,R)$, R is the measurement noise variance matrix.

Here is the specific UKF algorithm:

The state initialization given $\hat{X}_0 = E(X_0)$, $P_0 = E[(X_0 - \hat{X}_0)(X_0 - \hat{X}_0)^T]$.

Select sampling points and weights: $\{\chi_k(i), W_i^m, W_i^c\}$.

The nonlinear system model $\chi_{k+1|k}(i) = f(\chi_i, u)$ computes the mean and covariance of the predicted state:

$$\hat{X}_{k+1|k} = \sum_{i=0}^{L-1} W_i^m \chi_{k+1|k}(i) \tag{19}$$

$$P_{k+1|k} = \sum_{i=0}^{L-1} W_i^c [(\chi_{k+1|k}(i) - \hat{X}_{k+1|k})][(\chi_{k+1|k}(i) - \hat{X}_{k+1|k})]^T + \gamma_k Q \tag{20}$$

Measure sigma sampling, use $\hat{X}_{k+1|k}$ and $P_{k+1|k}$ to regenerate the sampling point set and weight $\{\chi_{k+1|k}(i), W_i^m, W_i^c\}$.

$$y_{k+1|k}(i) = h[\chi_{k+1|k}(i), u] \tag{21}$$

The prediction,variance and covariance are respectively:

$$\hat{Z}_{k+1|k} = \sum_{i=0}^{L-1} W_i^m y_{k+1|k}(i) \tag{22}$$

$$P_{ZZ} = \sum_{i=0}^{L-1} W_i^c [(y_{k+1|k}(i) - \hat{Z}_{k+1|k})][(y_{k+1|k}(i) - \hat{Z}_{k+1|k})]^T + \gamma_k R \tag{23}$$

$$P_{XZ} = \sum_{i=0}^{L-1} W_i^c [(y_{k+1|k}(i) - \hat{X}_{k+1|k})][(y_{k+1|k}(i) - \hat{X}_{k+1|k})]^T \tag{24}$$

Update the state and variance, and calculate the filter gain.

$$W_{k+1} = P_{XZ} P_{ZZ}^{-1} \tag{25}$$

$$\hat{X}_{k+1} = \hat{X}_{k+1|k} + W_{k+1}(Z_{k+1} - \hat{Z}_{k+1|k}) \tag{26}$$

$$P_{k+1} = P_{k+1|k} - W_{k+1} P_{ZZ} W_{k+1}^{-1} \tag{27}$$

The fuzzy adaptive unscented Kalman filter is shown in Figure 2.

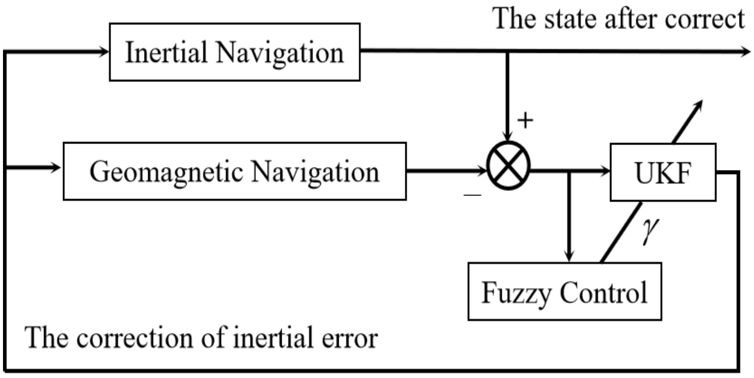

Figure 2: The Fuzzy Adaptive unscented Kalman Filter

III. SIMULATION AND DISCUSSION

The initial simulation conditions are as follows: The gyro drift is 0.01 (.)/h; The root mean square of gyro drift white noise is 0.01(.)/h; The initial position of the system is $X_0 = [50,30,0.35,0.35]^T$; The initial variance matrix of the system $P_0 = \begin{bmatrix} 0.1 & 0 & 0 & 0 \\ 0 & 0.1 & 0 & 0 \\ 0 & 0 & 0.1 & 0 \\ 0 & 0 & 0 & 0.1 \end{bmatrix}$ is a diagonal matrix; The variance matrices for the system's state noise and measurement noise are $Q = \begin{bmatrix} 0.05 & 0 & 0 & 0 \\ 0 & 0.05 & 0 & 0 \\ 0 & 0 & 0.001 & 0 \\ 0 & 0 & 0 & 0.001 \end{bmatrix}$ and $R = \begin{bmatrix} 1 & 0 \\ 0 & 0.001 \end{bmatrix}$, respectively. In the MATLAB R2018 environment, the simulation time of Monte Carlo is 100s. The simulation results are as follows:

Table 2: Filter Performance Comparison

Filter	RMS (errors)	Time (s)
EKF	0.12863	0.08362
UKF	0.11953	0.26742
FUKF	0.11176	0.47879

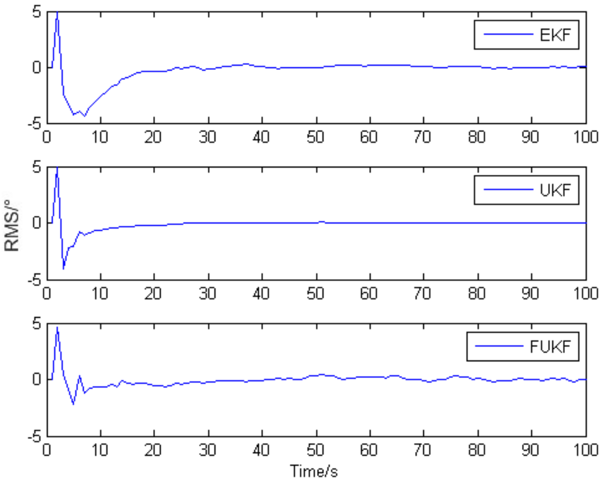

Figure 3: The curve of RMS error

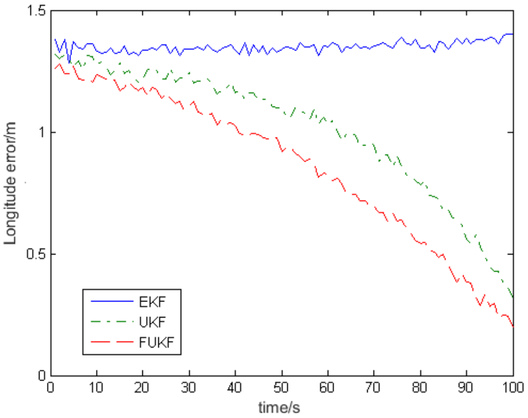

Figure. 4: The Curve of Longitude Error

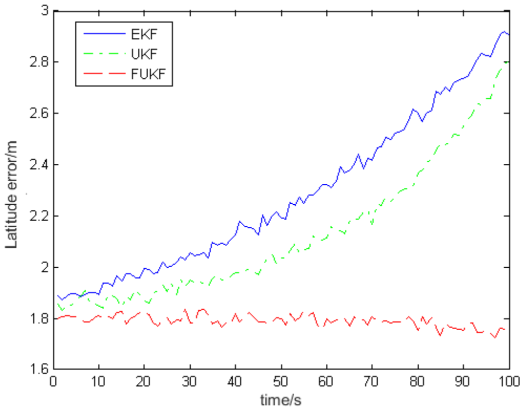

Figure. 5: The Curve of Latitude Error

It can be seen from Table 2 that compared with the EKF and UKF filtering algorithms, the fuzzy adaptive filtering algorithm has a smaller filtering error and larger calculation amount, resulting in increased calculation time.

Figure 3 shows that the FUKF filtering algorithm has fast convergence and a minimal filtering error. The Figures 4 and 5 show that the FUKF filtering algorithm can effectively suppress filtering divergence, with stable performance, and further improve the filtering effect of navigation system. In 100s, the system error remains within the range of the navigation accuracy. It is obvious that the model error can be successfully reduced by using the time-varying noise statistical estimator to estimate and correct the statistical features of system noise and observation noise in real time.

IV. CONCLUSION

The fuzzy adaptive unscented Kalman filtering approach suggested in this article modifies the model's noise variance matrix "online" in order to update the estimated mean square error and filtering gain. Additionally, it can handle the non-local impacts of UT transformation by adaptively adjusting the scaling factor of the weights in sigma sampling. The results show that the fuzzy adaptive Kalman filter is suitable for the inertial/geomagnetic integrated navigation system, and the measurement noise of the model is adaptive. When the nonlinearity is severe, this can effectively solve the issue of filtering divergence in the integrated navigation system.

ACKNOWLEDGEMENTS

The authors acknowledge the Natural Science Foundation of Liaoning (Grant: 2021-YKLH-03).

Data sharing agreement

The corresponding author will provide the datasets used and/or analyzed during the current work upon reasonable request.

Declaration of Conflicting Interests

The author certifies that there are no possible conflicts of interest in this article's research, writing, and/or publishing.

REFERENCES

1. Yingjing. Guo, Fang. Kong, Manlin. Zhang and Wenhong. Lyu (2020) Review of integrated navigation system for AUV, Navigation Positioning. Timing.,7 (5): 107–119.
2. Wenxuan. Fang, Dianwei.Cong(2022) Status and development of multi-source information fusion technology for satellite/Inertial/visual integrated navigation, Radio Engineering., 52 (10): 1813-1820.
3. Yixian. Zhu, Ling. Zhou (2021) Fuzzy Adaptive Filtering Algorithm Used in Autonomous Underwater Vehicle Integrated Navigation System, Journal of Nantong University., 20 (1): 34–39.
4. Julier S.Uhlmann, Durrant W H F(2020) A New Method for the Nonlinear Transformation of Mcans and Covariance in Filters and Estementors, IEEE Transacts on Automatie Control., 45 (3): 477-482.
5. Qiang. Fu, Hongyue. Zhao, Xiyan. Sun and Yuanfa. Ji (2020) Application research of improved strong tracking UKF algorithm in integrated navigation, Computer Simulation., 38 (2): 29-33.
6. Ping. Huang, Ting. Sun, Yanlong. Tong (2018) UKF integrated navigation algorithm based on adaptive simplex sampling, Systems Engineering and Electronics., 40 (7): 1567- 1572.
7. Haykin S(2002)Kalman Filtering and neural networks, John Wiley & Sons Inc.
8. Luying. Zhu, Weiwei. Sun, Chengming. Liu and Zhaowei. Sun(2022) Research on federal UKF algorithm for multi-sensor integrated navigation system, Journal of Electronic Measurement and Instrumentation., 36 (7): 91-98.
9. Xiaojie. Ma, Xueyuan. Lin, Qiaoyan. Sun and Xiangguang. Chen (2021) Improved UKF algorithm for BDS/SINS integrated navigation system, Journal of Geodesy and Geodynamics., 41 (4): 351-356.
10. Wangyan. Qiu, Rongbing. Li, Jianye. Liu(2020) Research on GNSS/MINS integrated navigation algorithm of general aviation based on improved adaptive fading kalman filter, Electronic Measurement Technology., 43 (10): 95-100.
11. Mehrnaz Poostpasand.Reza Javidan(2018) An adaptive target tracking method for 3D underwater wireless sensor networks,Wireless Networks., 24: 2797-2810.
12. Xiaobin. Xu, Minzhou. Luo, Zhiying. Tan and Min. Zhang (2019) Measured accuracy improvement method of velocity and displacement based on adaptive Kalman filter, Sensor Review., 39 (5): 708-715.

A Study on the Possibility of Utilizing Coffee Waste as a Recycled Resource Material using Ultrasonic Extraction Method

Taeyeob Lee, Yuri Kangσ & Woonjung Kim

University of Hannam

ABSTRACT

In this study, in order to confirm the potential of coffee waste as a recyclable resource material, the caffeine content of coffee waste and the effective active ingredients of coffee waste extract were confirmed using an ultrasonic extraction method. In order to conduct a preliminary experiment to determine whether extraction of coffee waste affects caffeine reduction, ultrasonic extraction was performed after immersion at room temperature for 48 hours at ethanol content of 0%, 30%, 50%, 70%, and 100%. The coffee waste recovered after extraction were analyzed for active ingredients using GC-MS.

Except for the coffee waste after extraction with 100% ethanol, almost no components other than caffeine were detected in the coffee waste recovered after extraction by ethanol content. As a result of quantitative analysis of caffeine in coffee grounds using LC-MS, a caffeine reduction rate of 72.1% was confirmed in the coffee grounds recovered after ultrasonic extraction with 70% ethanol.

Keywords: coffee waste, recycle, caffein, ultrasonic extraction, decaffein.

Classification: DDC Code: 663.4

Language: English

Great Britain
Journals Press

LJP Copyright ID: 392924
Print ISSN: 2631-8474
Online ISSN: 2631-8482

London Journal of Engineering Research

Volume 23 | Issue 5 | Compilation 1.0

A Study on the Possibility of Utilizing Coffee Waste as a Recycled Resource Material Using Ultrasonic Extraction Method

Taeyeob Lee[α], Yuri Kang[σ] & Woonjung Kim[ρ]

ABSTRACT

In this study, to confirm the potential of coffee waste as a recyclable resource material, the caffeine content of coffee waste and the effective active ingredients of coffee waste extract were established using an ultrasonic extraction method. To conduct a preliminary experiment to determine whether extraction of coffee waste affects caffeine reduction, ultrasonic extraction was performed after immersion at room temperature for 48 hours at ethanol content of 0%, 30%, 50%, 70%, and 100%. The coffee waste recovered after extraction was analyzed for active ingredients using GC-MS. Except for the coffee waste after extraction with 100% ethanol, almost no components other than caffeine were detected in the coffee waste recovered after extraction by ethanol content. As a result of quantitative analysis of caffeine in coffee grounds using LC-MS, a caffeine removal rate of 72.1% was confirmed in the coffee grounds recovered after ultrasonic extraction with 70% ethanol.

As a result of a preliminary experimental study, this study was conducted to confirm whether repeated re-extraction removed more than 90% of the caffeine content in the coffee waste and met the decaffeination standard. Based on the results of a preliminary experiment that confirmed the highest caffeine reduction rate in ultrasonic extracted coffee waste with 70% ethanol content, extraction was repeated 1 to 3 times using coffee waste with 70% ethanol content in the same manner as the preliminary experiment. As a result of quantitative analysis of caffeine in coffee waste using LC-MS in this experiment, a high reduction rate of 99.5% of caffeine content was confirmed to be removed from coffee waste recovered by repeated extraction with 70% ethanol three times.

Keywords: coffee waste, recycle, caffein, ultrasonic extraction, decaffein.

Author α σ: Department of Cosmetic science, University of Hannam, Daejeon, 34430, Korea.
ρ: Department of Chemistry, University of Hannam, Daejeon, 34430, Korea.

I. INTRODUCTION

The development of the food industry and food processing technology, along with the improvement of the standard of living of modern people, has shaped the coffee culture [1, 2, 3]. Coffee has become an essential item in the preferences of contemporary individuals, to the extent that it is often referred to as the "second water"[4]. How to make a cup of Americano, coffee is extracted using water, roasted coffee beans, The seeds of the coffee tree's fruit[5].

During the coffee extraction process, coffee waste, which refers to the leftover residues after the coffee extraction process, is generated. When making a cup of coffee, approximately 15 grams of coffee beans are used, with 14.7 grams being discarded, and 0.3 grams, which is 2%, is consumed as a beverage [6]. Coffee waste is generated worldwide at a rate of 10 million tons annually, and the amount of coffee waste is increasing by coffee consumption. In 2019, an 149,038 tons of coffee waste were produced [7, 8]. If such coffee waste is incinerated or landfilled without recycling, it incurs an annual cost of KRW 35 billion [9. 10].

Decaffeination refers to removing caffeine from coffee beans, cocoa, tea leaves, and other substances that contain caffeine. Therefore, decaffeinated coffee typically includes 1-2% of the original caffeine component, making it suitable for pregnant women, diabetes patients, and individuals with sensitive stomachs, and it is also known as 'caffeine-free' coffee [11]. The international standard for decaffeinated coffee is that more than 97% of caffeine is removed. Therefore, even in decaffeinated coffee, a small amount of caffeine may still be contained [12]. Caffeine is a compound formed by combining 'Coffee' with '-ine,' representing an alkaloid substance that collectively refers to essential organic compounds within plant organisms. Alkaloid substances often exhibit significant physiological and pharmacological effects, with notable examples including nicotine, morphine, and caffeine. Caffeine acts to stimulate the central and peripheral nervous systems, clearing the mind and increasing concentration and work ability [13, 14].

Therefore, caffeine may have some benefits for adults, but its impact on the central nervous system of children has not been sufficiently researched yet. The central nervous system of children is still in development, raising concerns about the potential side effects and health implications of caffeine [15]. Caffeine can be absorbed through the skin, so caution is necessary when using caffeine-containing substances in items for children, such as educational aids.

Research on the utilization of coffee waste includes studies on artificial cover material manufacturing for sewage sludge using coffee sludge [16], activated carbon adsorbents [17], eco-friendly composting [18], wastewater treatment [19], coffee soap and air freshener manufacturing [20] etc., but the actual amount of coffee grounds used can be said to be minimal.

Furthermore, recently, some clay products for children have incorporated recycled materials, including coffee waste. However, existing clay products made with recycled coffee waste have limitations for use by children due to factors such as caffeine content. Therefore, teaching aids made from recycled coffee grounds should minimize the caffeine content in consideration of the age and sensitivity of children. Therefore, this study aims to confirm the reduction of caffeine by using repeated extraction of coffee grounds and the decaffeination potential of coffee grounds to confirm their safety and potential as a recycled resource and as a recycled material.

II. EXPERIMENT

2.1 Materials

The coffee waste used in this study was provided in the form of coffee waste powder from Harmony Co., Ltd. in February 2023 and stored at room temperature for testing.

2.2 Extraction Condition Experiment for Coffee Waste I

Distilled water and ethanol were used as solvents in Experiment I for extraction of coffee waste. The volume was set at 300 ml, with a sample weight of 30 g. Ethanol was used in varying concentrations of 0%, 30%, 50%, 70%, and 100%, and extraction was carried out at room temperature for 48 hours after immersion. The ultrasonic extraction conditions involved using an extraction device (ULTRA SONIC, BMWORKS, Daejeon, Korea) at 20°C, operating at 20 kHz for 30 minutes. The extracted solution was subjected to decompressed filtration through a 5-8 ㎛ filter (Hyun Dai, Micro, Korea) using a vacuum pump (DOA-P704-AC, GAST Manufacturing Inc, U.S.A). After the filtration, the coffee extract was dried in a 60°C Coven for 48 hours and stored at 4°C for GC-MS and caffeine analysis.

2.3 Repeated Extraction Experimental Conditions for Coffee Waste Ⅱ

For the repeated extraction of coffee waste in Experiment II, the same solvents, water, and ethanol, were used as in Experiment I. For the ultrasonic extraction conditions for Experiment II, the volume was set at 300 ㎖, with a sample weight of 30 g, and 70% ethanol was used. The extraction was carried out in the same way as Experiment 1 at room temperature for 48 hours after immersion. After filtration, the coffee waste was dried in a 60°C oven for 48 hours, and the process of obtaining the coffee waste extraction material was repeated 1-3 times.

2.4 Caffeine Quantification in Coffee Waste Using LC-MS

The caffeine content in coffee waste was analyzed using HPLC (Agilent 1290). After a 50 mg sample was measured and injected into a vial, 2 ml of methanol was added, and sonication was carried out for 60 minutes. The analysis was conducted using a 0.45 ㎛ PVDF syringe filter. An LC column, Kinetex 2.6 ㎛ EVO C18 100Å 2.1×100 mm, was used. The column temperature was maintained at 40°C, with a flow rate of 0.300 mL/min, and an injection volume of ㎕. The MS was conducted under a gas temperature of 300°C, a drying gas flow rate of 10 L/min, and a nebulizer pressure of 45 psi. The LC-MS analysis method for this experiment, was carried out in the same way.

2.5 Effective Active Ingredients Analysis in Coffee Waste Extract Using GC-MS

For the analysis of effective active ingredients in the coffee waste extract for experimentl, GC-MS (Gas chromatography-mass spectrometry) was used. For GC analysis, column (Agilent 19091S-433) was used for 45 minutes using HP-5ms (30 m x 250 ㎛ x 0.25 ㎛). The injection volume was 1 ㎕, the carrier gas was He, and the flow rate was maintained at 10 ㎖/min. The oven temperature was maintained at an initial temperature of 40 °C for 3 minutes and then increased by 5 °C/min to a final temperature of 300 °C. After doing so, the analysis was carried out while maintaining it for 1 minute.

III. RESULTS AND CONSIDERATIONS

The results for the coffee waste recovered after ultrasonic extraction in this study are as follows. The coffee waste recovered after extraction in experiment I was labeled as original materials (ORG) and A to E, depending on the ethanol content.

The coffee waste recovered after extraction with 0% ethanol ultrasonic extraction is labeled as A, 30% ethanol as B, 50% ethanol as C, 70% ethanol as D, and 100% ethanol as E, as shown in <Table 1>.

Table 1: Numbering Based on the Ethanol Content of the Extract by Ultrasonic Extractor

DW : Ethanol	Ultrasonic extractor
100 : 0	A
70 : 30	B
50 : 50	C
30 : 70	D
0 : 100	E

In Experiment II, depending on the number of extractions, the recollected materials were labeled as original materials (ORG) and G1 to G3.
The coffee waste recovered after ultrasonic extraction with 70% ethanol is labeled as G1 for the first extraction, G2 for the second extraction, and G3 for the third extraction, as shown in <Table 2>.

Table 2: Numbering Based on the Ethanol Content of the Extract by Ultrasonic Extractor

DW : Ethanol	Number of Repeated Extractions	Ultrasonic extractor
30 : 70	1 time	G1
	2 times	G2
	3 times	G3

3.1. Caffeine Content Analysis of Coffee Waste Using LC-MS

The caffeine content of coffee waste analyzed using LC-MS is as follows.

As shown in <Table 3 & Figure 1>, the 70% ethanol ultrasonic coffee waste exhibited the lowest caffeine content at 404.89 µg/g, showing a 72.1% reduction in caffeine compared to the initial caffeine content of the ORG <Table 4>.

Table 3: LC-MS Quantitative Analysis Results for Caffeine in the Coffee Waste Extract by the Ultrasonic Device Used in the Experiment

Sample	mg	g	Caffeine Content in 2 ml of Extracted Methanol (µg)	A 10-Fold Dilution factor	Final Concentration µg/g
ORG	46.9	0.0469	6.809	68.093	1451.9
A	47.4	0.0474	6.676	66.763	1408.5
B	53.4	0.0534	3.976	39.760	744.57
C	50.5	0.0505	3.841	38.411	760.61
D	50.7	0.0507	2.053	20.528	404.89
E	51.3	0.0513	6.650	66.504	1296.4

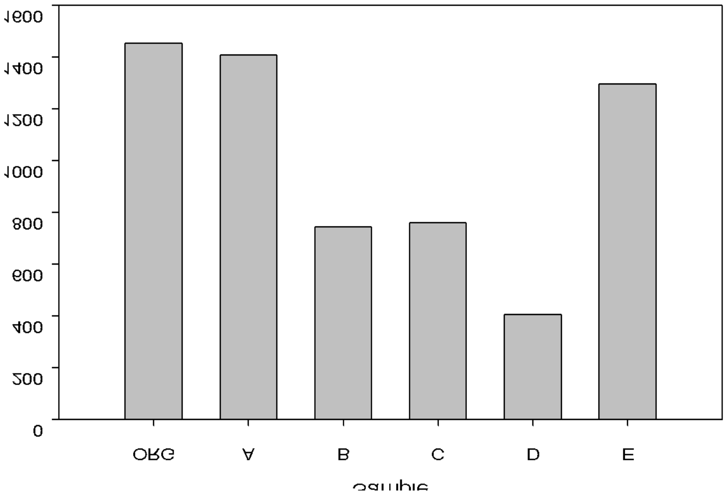

Figure 1: Comparison of LC-MS Quantitative Analysis Results of Caffeine in Coffee Waste Extract by Ultrasonic Device Used in the Experiment;

Table 4: Final Concentration Reduction Rate as a Result of LC-MS Quantitative Analysis of Caffeine in the Coffee Waste Extract by the Ultrasonic Device Used in the Experiment

Sample	Final Concentration (µg/g)	Reduction Rate (%)
ORG	1451.9	-
A	1408.5	3.00
B	744.57	48.7
C	760.61	47.6
D	404.89	72.1
E	1296.4	10.7

3.2 GC-MS Analysis of Effective Active Ingredients in Coffee Waste

The GC-MS analysis results of effective ingredients in the recovered coffee waste after extraction are presented in <Table 5>. No other compounds were detected in the coffee waste recovered after ultrasonic extraction except for caffeine. However, in the coffee waste recovered after extraction with 100% ethanol, compounds such as 2,4-Dimethyl-1-heptene, n-hexadecanoic acid, and Benzene were detected. The GC-MS results graph of the coffee waste recovered after extraction, based on the ethanol content, is shown in Figure 2.

Table 5: Results of GC-MS Analysis of Coffee Waste Extract by Ultrasonic Extractor

(Unit: Area %)

Extract Active Ingredient	Caffeine	2,4-Dimethyl-1-hEptene	n-Hexadecanoicacid (Palmitic Acid)	Benzene
A	100	-	-	-
B	100	-	-	-
C	100	-	-	-
D	17.7	-	-	-
E	19.3	13.4	1.88	10.4

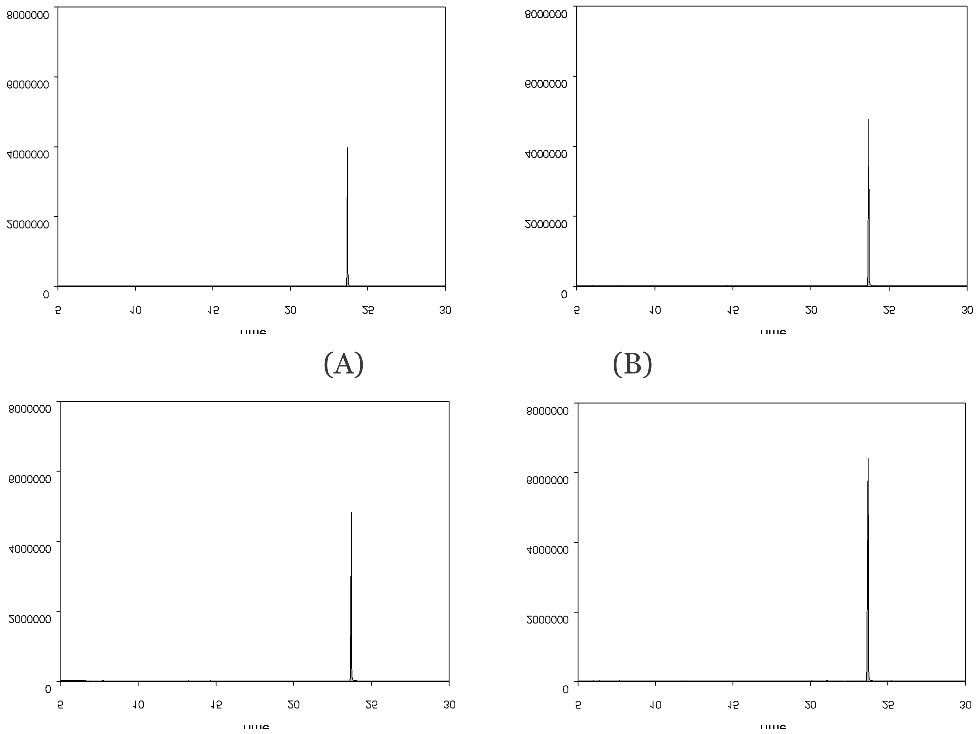

(A) (B)

(C) (D)

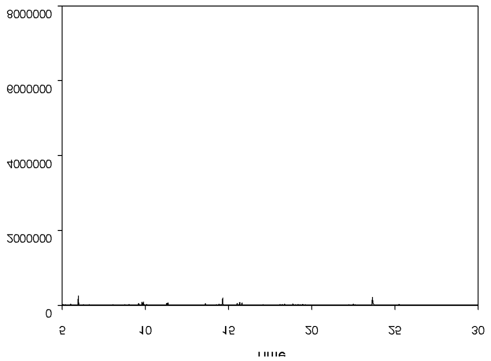

(E)

Figure 2: Comparison of GC-MS Analysis Results of the Coffee Waste Extract by the Ultrasonic Extractor

3.2 Quantitative Analysis Results of Caffeine Using LC-MS for This Experiment

The caffeine content in the coffee waste recovered after ultrasonic extraction is as follows.

As shown in <Table 7 and 8>, a significant caffeine reduction rate of 99.5% was observed in the coffee waste obtained from ultrasonic extraction using 70% ethanol after three times of repeated extraction. The Korea Food and Drug Administration has confirmed that decaffeination, with 90% removal of caffeine, can be achieved with just two repeated experiments of coffee waste extraction <Figure 3>.

Table 6: LC-MS Quantitative Analysis Results for Caffeine in the Coffee Waste Extract by the Ultrasonic Device Used in the Experiment

Sample	mg	g	Caffeine Content in 2 Ml of Extracted Methanol (μg)	A 10-Fold Dilution Factor	Final Concentration μg/g
ORG	53.7	0.0537	12.8	128.1	2386.1
G1	50.0	0.0500	3.22	32.22	644.49
G2	52.0	0.0520	3.55	3.550	68.230
G3	50.6	0.0506	0.59	0.590	11.730

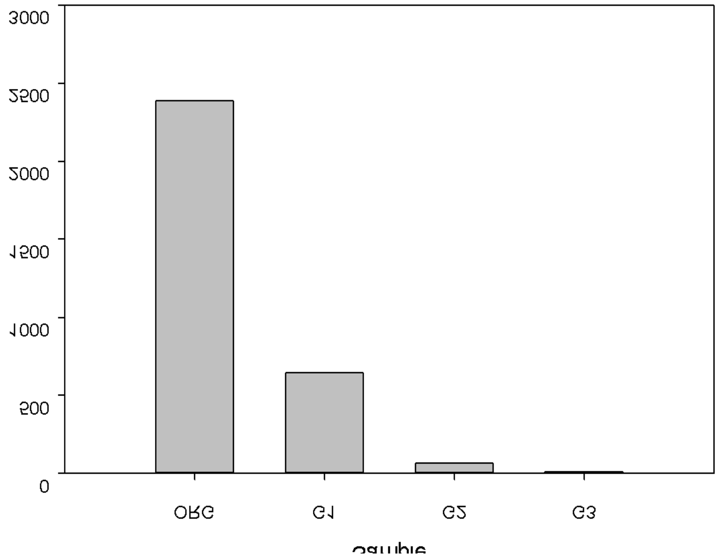

Figure 3: Comparison of LC-MS Quantitative Analysis Results of Caffeine in Coffee Waste Extract by Ultrasonic Device in the Experiment;

Table 7: Final Concentration Reduction Rate as a Result of LC-MS Quantitative Analysis of Caffeine in the Coffee Waste Extract by the Ultrasonic Device in the Experiment

Sample	Final Concentration (μg/g)	Reduction Rate (%)
ORG	2386.1	-
G1	644.49	73.0
G2	68.230	97.2
G3	11.730	99.5

VI. CONCLUSION

This study utilized ultrasonic extraction to investigate the caffeine content and effective active ingredients in coffee waste, confirming its potential as a recyclable resource The ultrasonic extraction method was used for coffee waste extraction, and preliminary experiments were conducted under conditions ranging from 0% to 100% ethanol content. The GC-MS analysis results of effective ingredients in coffee waste revealed that, except for the coffee waste recovered after 100% ethanol extraction, hardly any other components were detected in coffee waste recovered after extraction with different ethanol contents. The LC-MS analysis of caffeine content revealed a 72.1% reduction in caffeine in the coffee waste recovered after 70% ethanol ultrasonic extraction, compared to the coffee waste without ultrasound extraction.

Furthermore, additional research was conducted to confirm whether the caffeine content within coffee waste could be reduced by over 90% to meet decaffeination standards. The re-extraction was performed using 70% ethanol, which showed the highest caffeine reduction rate among the ethanol concentration ranges. In addition, repeated extraction was performed 1 to 3 times, and the extraction method was ultrasonic extraction conducted under preliminary experimental conditions. The quantitative analysis of caffeine in coffee waste using LC-MS revealed a high caffeine removal rate of 99.5% in the coffee waste recovered after three times repeated extractions with 70% ethanol. As a result of this study, the potential for decaffeination through the repeated ultrasonic extraction of coffee waste was confirmed, and this verified its potential as a recyclable resource material.

ACKNOWLEDGEMENT

This work was supported by the National Research Foundation of Korea(NRF) grant funded by the Korea government(MSIT) (RS-2023-00281517), and 2023 Local University Revitalization Project funded by the National Research Foundation of Korea.

REFERENCES

1. J. Y. Choi, A Study on Purchasing Characteristics and Consumer Sat is faction on Health Functional Beverage according to Food-related Lifestyle Hotel Resort Research, 12(1), pp.179-196. (2012).
2. Scott K, The sweet and the bitter of mammalian taste, Curr Opi Neurobiol 14: pp. 423-427, (2004).
3. Emile Peynaud, The Taste of wine, The wine appreciation guild, pp. 31-114, 1987.
4. H. U. Park, H. E. Lee, World Coffee Industry Trends, World agricul ture, No. 145, pp. 97-116, (2012).
5. Robert HR, Barone J J. Biological effects of caffeine-history and use. Food Technol, 37:32-39.(1983).
6. S. W. Kim. A Study on the Utilization ofSpentCoffeeasAnimalFeed. ThesisKonkukUniversity.p11-13. (1990).
7. I. C. O (International Coffee Organization) resaerch, rade Statistics Tables, World coffee consumption. https://www.ico.org/trade_statistics.asp?section=Statistics. (2021)
8. Y. J. Park, 5 trend changes and prospects in the coffee industry, Korea Economic Review, Vol. 848, No. 0, Hyundai Research Institute, 1p, (2019),
9. K. M. Kim, Y. S. Park. A plan to turn bio energy into fuel by establishing a coffee grounds collection system. See p.7 (2020).

10. National Assembly Research Service. (Ministry of Foreign Affairs > News, Notices > Press Release, (2021).
11. Zabot GL. Decaffeination using supercritical carbon dioxide. In: Green Sustainable Process for Chemical and Environmental Engineering and Science, Elsevier, Amsterdam, Nederlanden, p 255-278 (2020).
12. KCS (Korea Customs Service). Coffee (bean) import trends in 202 2. Available from: https://www.customs.go.kr/streamdocs/view/sd;stream%20amdocsId=72059269162294321 , Accessed May. 10, (2023).
13. Pohler, H., Caffeine intoxication and addiction, J. Nurse Pract., 6, 49-52, (2010).
14. O'Neil, M. J., The Merck Index - An encyclopedia of chemicals, drugs, and biologicals. 14th edition., White house Station, NJ, Merck and Co., Inc, (2013).
15. J. E. Lee, W. Huh, E. J. Choi, Pattern Analysis of High-caffeine Energy Drink Consumption and Adverse Effects among College Students in a University. Yakhak Hoeji. 57(2), (2013).
16. G. Y. Lee, H. H. Hyeon, T. J. Ryu, J. Y. Yoon, W. S. Lee, C. H. Lee, K. J. Park, "Re-evaluation of artificial cover for sewage sludge using Busan phosphorus gypsum and coffee sludge". Journal of the Korean Society of Waste and Resource Circulation 2011, pp.224-226, (2011).
17. H. Y. Kang, "Adsorption characteristics of activated carbon prepared from coffee grounds", PhD thesis, Chonnam National University Graduate School, (2007).
18. H. S. Kim, "Eco-friendly composting using coffee by-products", master's thesis, Kwangwoon University Graduate School of Environmental Studies, (2012).
19. C. H. Song, C. H. Lee, T. L. Huh, J. H. Ahn, H. C. Yang, Development of substrates for the production of basidiocarps of Flammulina velutipes. Korean J Mycol.21:212-216, (1993).
20. E. J. Song, J. Y. Kim, S. Y. Lee, S. Y. KIM, K. B. W. R. Kim, S. J. Kim, S. Y. Yoon, S. J. Lee, C. J. Lee, D. H. Ahn, Effect of roasted ground coffee residue extracton shelf-life and quality of salted mackerel.J Korean SocFood SciNutr.38:780-786, (2009).